AJS American Journal of Science
publishing earth-sciences research since 1818

Wintsch, R. P., Wathen, B. A., McAleer, R. J., Walters, J., & Matthews, J. A. (2024). Deformation by Pressure Solution and Grain Boundary Sliding in a Retrograde Shear Zone in Southern New England, USA. *American Journal of Science*, *324*, 17. https://doi.org/10.2475/001c.125064

Science Paper

Deformation by Pressure Solution and Grain Boundary Sliding in a Retrograde Shear Zone in Southern New England, USA

Robert P. Wintsch[1,2,3][a], Bryan A. Wathen[3,4], Ryan J. McAleer[5], Jesse Walters[6], Jessica A. Matthews[3,7]

[1] Department of Earth and Environmental Sciences, Wesleyan University, [2] State Geological and Natural History Survey of Connecticut, [3] Department of Earth and Atmospheric Sciences, Indiana University, [4] Lewis G. Weeks Hall for Geological Sciences, University of Wisconsin–Madison, [5] Florence Bascom Geoscience Center, U.S. Geological Survey, [6] Department of Earth Sciences, University of Graz, [7] Cheveron Technical Center, Louisiana St., Houston

Keywords: diffusion creep, pressure solution, shear zone, retrogression, deformation mechanisms, dissolution-precipitation, recrystallization

https://doi.org/10.2475/001c.125064

American Journal of Science

Vol. 324, 2024

Alleghanian phyllonites in a shear zone in southern New England were formed by the retrogression and hydration of a high-grade Acadian pelitic schist. The retrogression was locally incomplete, resulting in both heterogeneous mineralogy and mineral compositions, and in many arrested reaction textures. These features, documented by backscattered electron and element map imaging, and by $^{40}Ar/^{39}Ar$ dating, provide a record of the processes active as the schist was converted to a phyllonite. On the margins of the shear zone relic biotite and garnet grains survive but are partially replaced by chlorite. Relic high-grade muscovite flakes containing up to 35 % paragonite (pg) also persist but are entrained in swarms of pg-poor muscovite flakes producing folia with an anastomosing network of muscovite grains of variable composition. Single crystals of pg-rich muscovite are truncated by muscovite in successively younger cross-cutting folia that contain decreasing pg contents, falling to <5% pg in the youngest folia. In the core of the shear zone all high-grade minerals are destroyed, but recrystallization continues with earlier greenschist facies folia replaced by lower grade and pg-poorer muscovite in younger folia. Muscovite grains in truncated folia are commonly kinked and selective recrystallization of muscovite in kink bands to pg-poor-compositions demonstrates that strain energy helped drive recrystallization. The boundaries of these new pg-poor muscovite folia are sharp, and truncations indicate that grain boundary sliding (GBS) involved dissolution. GBS also enabled folding by flexural slip along muscovite grain boundaries. Fold amplitudes increased as chlorite dissolved from fold limbs precipitated in fold hinges producing crescent-shaped saddle-reef-like structures. Together these observations of truncation and replacement by dissolution and precipitation demonstrate that pressure solution and GBS facilitated both the formation of the phyllonitic shear zone and slip along it.

1. INTRODUCTION

Retrograde shear zones are common worldwide where they record important parts of the exhumation history of mountain belts (Fossen & Cavalcante, 2017). They typically contain well developed foliations defined by phyllosilicates that are relatively weak (Kronenberg et al., 1990), and that replaced higher grade and commonly stronger minerals (Ceccato et al., 2022; Wintsch et al., 1995). This evolution toward weakening leads to strain localization and fault reactivation (e.g., Diener et al., 2016; Samsu et al., 2023). It may also produce or enhance ductility contrasts that lead to the development of stretching faults and stretching fault systems (Bailey et al., 2004; Fossen & Cavalcante, 2017; Means, 1989; Scharf et al., 2013).

Despite this progress questions about the dominant deformation mechanisms operating, and the role and the availability of H_2O in micaceous shear zones persist (Stenvall et al., 2020; Tenczer et al., 2006). The mineralogy and microstructures in retrograde shear zones can be especially revealing because these fault rocks can retain textural evidence of retrograde reaction and deformation mechanisms (e.g., McAleer et al., 2017; Nosenzo et al., 2023; Wiest et al., 2020), but more work is necessary to identify details of how these shear zones deform. Of the several mechanical and chemical deformation mechanisms involved in the production of strong foliations, those most commonly proposed

a Corresponding author: wintsch@iu.edu

are dislocation creep and pressure solution (Passchier & Trouw, 2005; Wallis et al., 2015; Wenk et al., 2020). With regard to phyllosilicates, experimental deformation of single crystals with orientations oblique to the shortening direction shows that these crystals are relatively weak, and that dislocation glide operates in the basal plane of mica flakes (Kronenberg et al., 1990). Experiments using natural and synthetic micaceous rocks show that increasing mica content and increasing mica grain contiguity greatly decrease rock strength (Mariani et al., 2006; Shea & Kronenberg, 1992, 1993; Tokle et al., 2023). However, evidence for dislocation glide in nature is not always strong (Bons, 1988; McNamara et al., 2024; Wallis et al., 2015), and the a- and b-axis preferred orientation anticipated for dislocation glide in muscovite (Mares & Kronenberg, 1993) is commonly absent (e.g., Wenk et al., 2020).

In contrast, most studies of naturally deformed rocks identify pressure solution processes as important deformation mechanisms in many crustal settings (e.g., Ceccato et al., 2022; De Caroli et al., 2024; Gratier et al., 2013; A. L. Lee et al., 2022; Rutter, 1983; Tulley et al., 2022; Wintsch & Yi, 2002). Evidence for this comes from (1) the truncation of grains in earlier fabrics by new minerals defining overprinting foliations (Wenk et al., 2020; Wintsch et al., 2005), (2) from minerals in foliations with new compositions compared to precursor minerals (Airaghi et al., 2017; McAleer et al., 2017; McWilliams et al., 2007; White & Johnston, 1981), and (3) from petrochronology, that is, the identification of younger ages of grains in succeeding foliations (Beaudoin et al., 2020; Oriolo et al., 2022; Torgersen et al., 2022; Villa et al., 2023).

The present contribution builds on these studies with detailed microstructural observations placed in metamorphic, geochronologic, and aqueous geochemical contexts to identify the metamorphic conditions and deformation mechanisms that operated in a belt of retrograde Alleghanian phyllonites in a shear zone in southern New England, USA (fig. 1). Our study takes advantage of the persistence of relic high-grade, Na-rich muscovite flakes from the protolith identified with element maps and electron microprobe analysis (EMPA) to help determine the relationships among different generations of muscovite grains in the retrograde phyllonites. These microstructures are compared to those expected from possible deformation mechanisms to determine the dominant mechanisms that operated there.

2. GEOLOGIC BACKGROUND

The retrograde East Derby shear zone (EDsz; 'shear zone' is not capitalized because the name is informal) in the southwestern New England Appalachians (fig. 1) cuts high-grade schists and gneisses accreted to the eastern margin of Laurentia in the early Paleozoic. The zone is characterized by a band of lower greenschist facies phyllonites from 0.5 to 1.0 km wide. The phyllonitic foliation dips steeply west and cuts at a small angle steeply east-dipping foliations in adjacent wall rocks (Fritts, 1965; Wathen et al., 2015). Outcrop-scale folds are not common, but where present the asymmetry of the folds suggests sinistral strike-slip translation as does the transposition of foliations and quartz veins into the dominant foliation (Wathen et al., 2015). In contrast, folds in the Wepawaug Schist (Growdon et al., 2013) and transposition of isograds in the Wepawaug Schist (fig. 2) suggest a component of dextral shear. This belt of phyllonites was originally interpreted as a stratigraphic unit correlating with the greenschist facies Ordovician pelitic Savin Schist to the south and east (fig. 2) around a NNE plunging Wepawaug Syncline (Fritts, 1962). However, Hatch and Stanley (1973) recognized that the phyllonites constituted a retrograde fault zone and are not part of any folded stratigraphy.

East of the EDsz lies the Early Devonian Wepawaug Schist that marks the southern-most exposure of Connecticut Valley Trough sediments (Hatch & Stanley, 1973; fig. 1B). The schist was metamorphosed during the Acadian orogeny in the Middle to Late Devonian. Sm-Nd ages of a garnet core and rim (~389 and ~380 Ma, respectively, Lancaster et al., 2008) and a U-Pb age of monazite (~388 Ma, Lanzirotti & Hanson, 1996) document this event. The rocks display a metamorphic field gradient toward the southwest from chlorite to staurolite-kyanite grade (Fritts, 1962, 1965) where metamorphic conditions reached ~650 °C and ~1.0 GPa (fig. 3B; Ague, 1994a, 1994b, 2002). The schist was exhumed to greenschist facies conditions in the early Carboniferous as established by $^{40}Ar/^{39}Ar$ amphibole and muscovite cooling ages of ~375 and ~365 Ma, respectively (Growdon et al., 2013; this study). The rocks and isograds were subsequently telescoped and shortened to ~30% in the late Paleozoic (green dashed line, fig. 2; Growdon et al., 2013).

West of the EDsz lies a complex of Ordovician and Silurian orthogneisses and paragneisses (Sevigny & Hanson, 1993, 1995). These were also metamorphosed to upper amphibolite facies in the Devonian as documented by U-Pb ages of garnet (~380 Ma) and monazite (395–375 Ma; Sevigny & Hanson, 1993, 1995), and of staurolite and monazite (400–380 Ma, Lanzirotti & Hanson, 1995, 1997). The gneisses show a metamorphic field gradient from regional staurolite + kyanite grade in NW Connecticut with metamorphic conditions reaching 700 °C and 1.0 GPa near the Waterbury and Bristol domes (fig. 1B; Hillenbrand et al., 2023, 2024) to about 650 °C and 0.7 GPa in the greater Bridgeport area (Matthews et al., 2008). West of the EDsz (fig. 2) the metamorphic field gradient shows an increase in metamorphic grade from regional staurolite-kyanite grade to sillimanite + muscovite followed by the disappearance of first staurolite and then kyanite to the southeast. These 'isograds' are extrapolated from the mapping of isograds in pelitic paraschists and gneisses primarily west of the Ansonia quadrangle (Matthews et al., 2008) into the feldspathic orthogneisses where these index minerals are lacking (dotted lines, fig. 2; Wathen et al., 2015). Rb-Sr, K-Ar, and $^{40}Ar/^{39}Ar$ cooling ages and a Triassic non-conformity show that the rocks were cooling from the Late Devonian through to exposure in the early Mesozoic (Clark & Kulp, 1968; Dietsch et al., 2010; Growdon et al., 2013; Moecher et al., 1997; Wheeler, 1937).

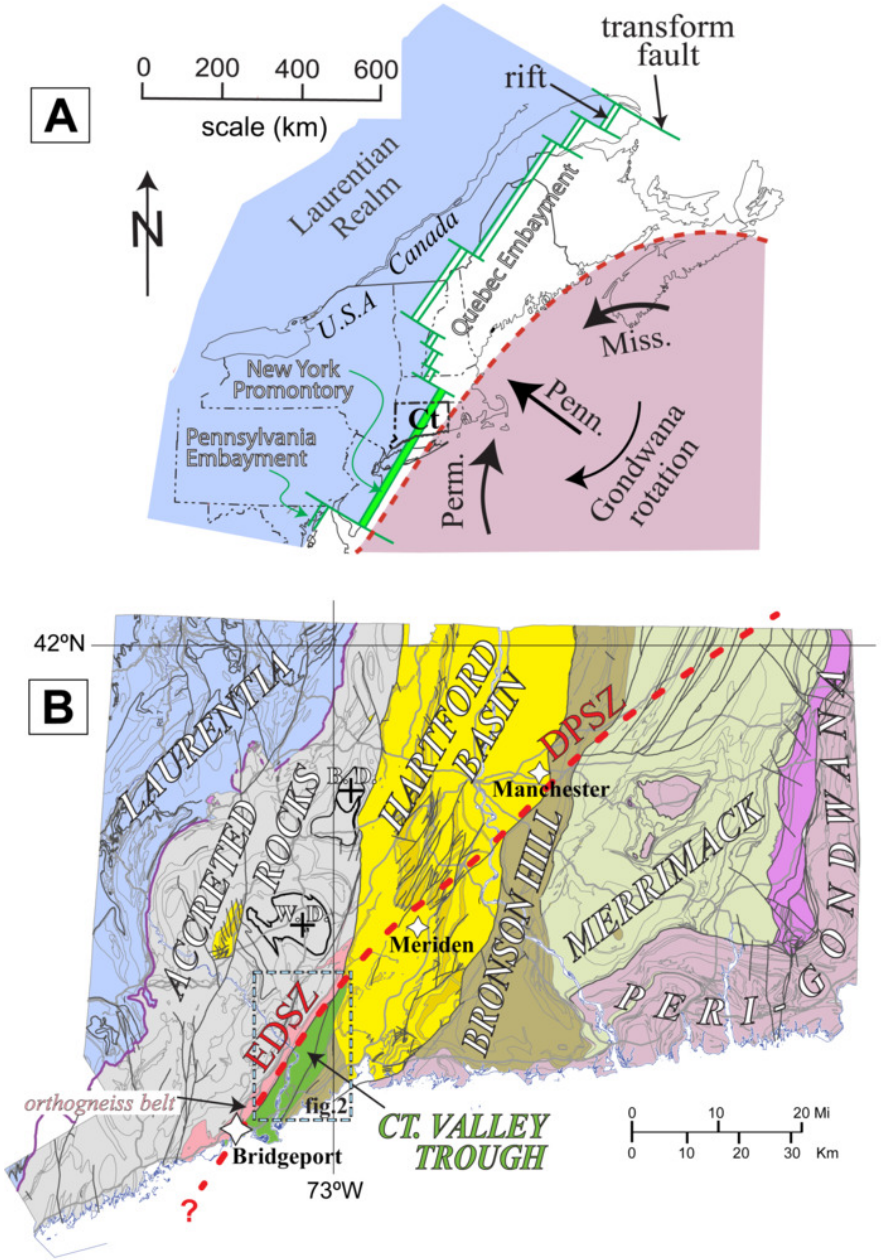

Figure 1. (A) Map of northeast North America (from Thomas, 2006) showing the locations of promontories and embayments in Laurentia (blue) created by rifting of the Rodinia supercontinent ~600 Ma producing rifts and transform faults (double and single green lines, respectively). The New York promontory is highlighted in green, and the location of Connecticut (Ct) is indicated. Gondwana (lilac) rotated clockwise during its late Paleozoic convergence with Laurentia (Hatcher, 2002). (B) Geologic terrane map of Connecticut (modified from Hibbard et al., 2006; Rodgers, 1985) showing Laurentia (blue), accreted rocks (gray), Connecticut Valley Trough (apple green), Bronson Hill terrane (brown), Merrimack belt (pale green), and peri-Gondwanan terranes (shades of lavender). Sediments (yellow) and volcanic rocks (ochre) lie in the down-faulted Hartford Basin. Bold dashed red line shows the trace of the East Derby shear zone (EDsz) with the possible extension to the Dobsonville Pond shear zone (DPsz) and brittle reactivation cutting the Hartford Basin near Meriden (Wintsch et al., 2003). B.D. and W.D. with + identifies the Bristol and Waterbury domes, respectively. Box identifies the location of figure 2.

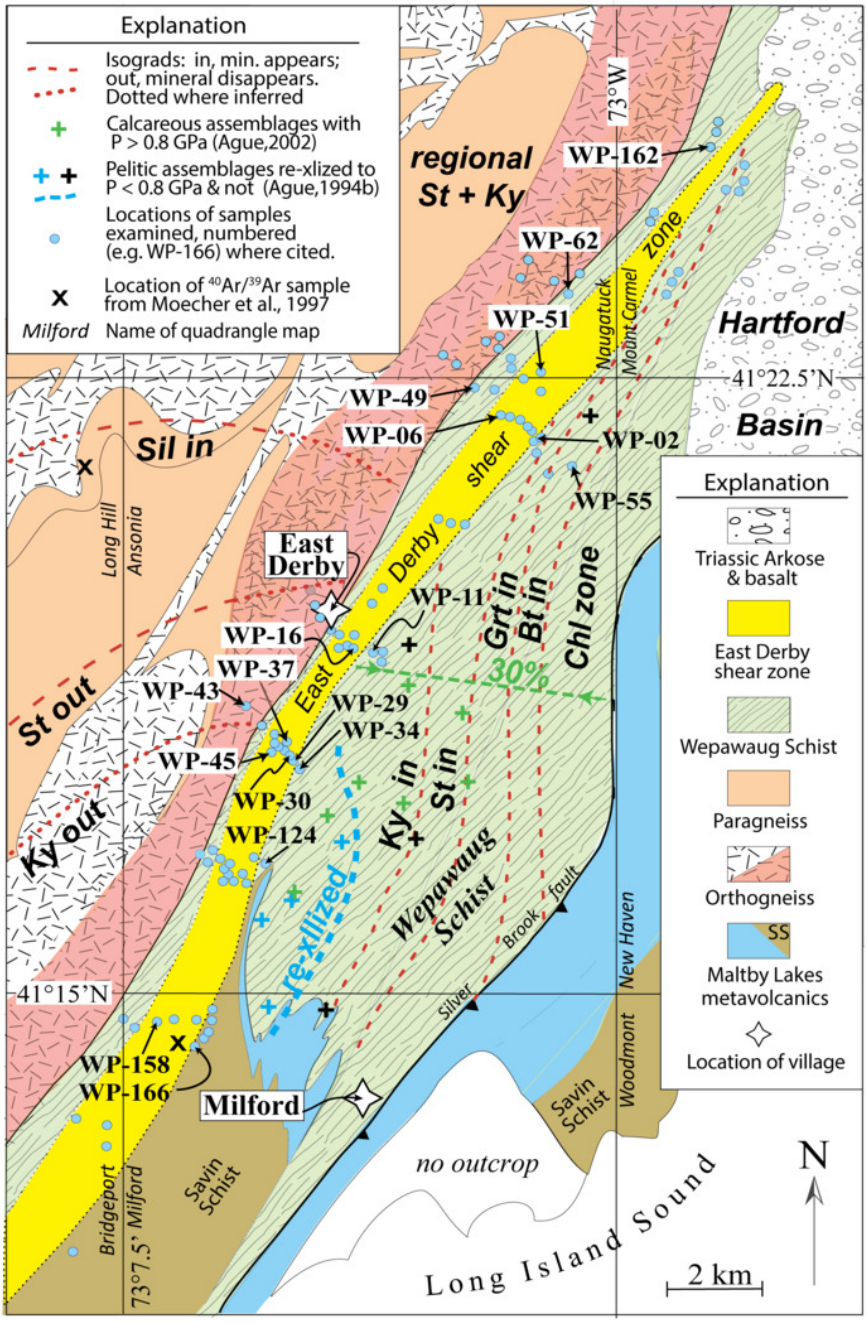

Figure 2. A generalized geologic map of southwest Connecticut (modified from Deasy et al., 2017; Fritts, 1965; Rodgers, 1985) showing the location of the East Derby shear zone (yellow) truncating rocks and isograds of the Wepawaug Schist (green) and high-grade orthogneisses (pink). Dashed red lines show the locations of metamorphic isograds (Ague, 1994a; Fritts, 1965; Matthews et al., 2008). Locations of samples with P ≥ 0.8 GPa in pelitic and calcareous rocks are indicated with black and green +, respectively. Kyanite zone pelitic samples with P < 0.8GPa are indicated with blue + (Ague, 1994b, 2002). Pale blue circles show the location of sample sites examined; those with sample numbers (e.g., WP-166) are described in this study and in Wathen (2020). Isograds west of the EDsz from Matthews et al. (2008). Stars give locations of villages. Abbreviations used here or in the following figures: Ab, albite; And, andalusite; Ap, apatite; Bt, biotite; C, chlorite; Grt, garnet; Ky, kyanite; Ms, muscovite; Pl, plagioclase; Q, quartz; Sil, sillimanite; St, staurolite.

3. METHODS

The field and laboratory methods described below have been employed to identify the deformation mechanisms that operated in the phyllonites of the retrograde EDsz and to establish a more detailed geological context for these rocks. The analytical work was conducted primarily at a scale <1mm to best identify the grain-scale processes that produced the foliations in these rocks.

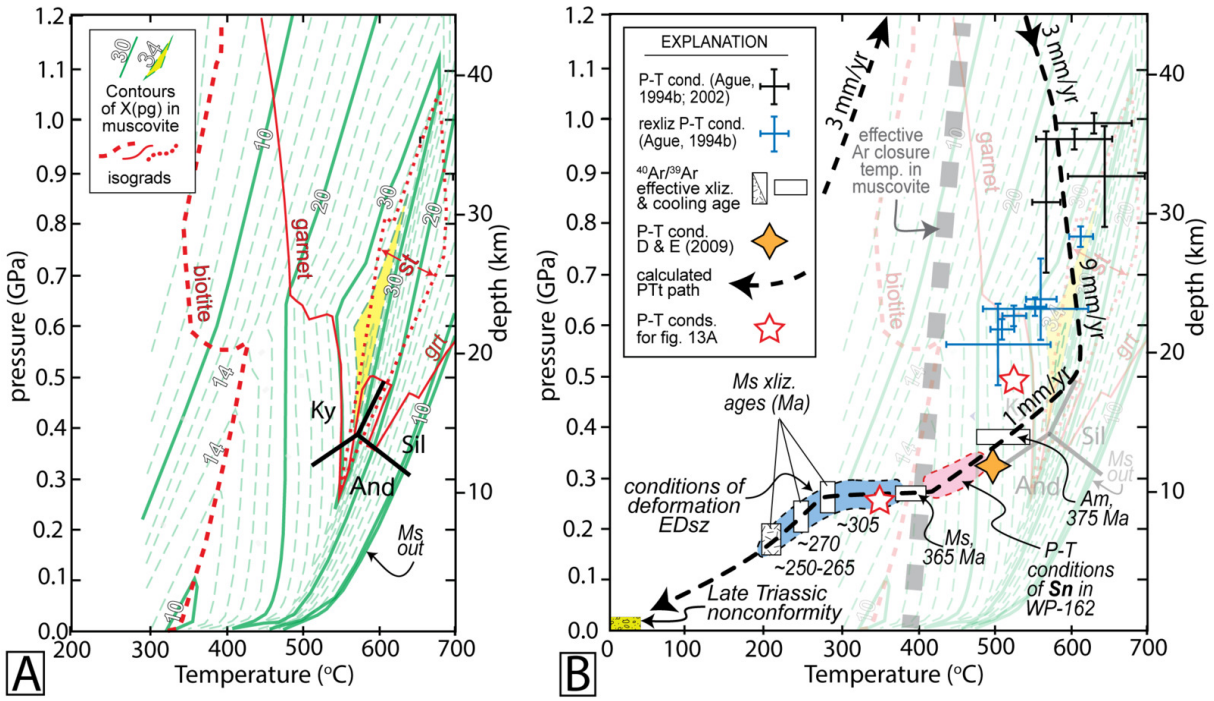

Figure 3. Pressure - temperature diagrams. (A) Diagram showing the stability fields of biotite, garnet, staurolite, and the aluminosilicates in the Wepawaug Schist of average chlorite-biotite zone composition calculated in a pseudosection using Perple_X (see Supplementary information). Green lines contour the paragonite (pg) component of muscovite, with a maximum of ~ 35 mole % in the staurolite field. (B) A pressure-temperature diagram showing the PTt path of rocks in the EDsz (bold black dashed line). Black and blue crosses show the PT conditions for kyanite-grade and recrystallized rocks, respectively, of the pelitic Wepawaug Schist with 2σ error bars (Ague, 1994b, 2002). Orange diamond shows calculated PT conditions from intersecting fluid inclusions (Dabrowski & Evans, 2009). The blue and pink ovoid fields show the P-T conditions of deformation in the EDsz and of fabric development in sample WP-162, respectively. The calculated closure temperature of Ar diffusion in muscovite is given by the bold dashed gray line. Red stars mark the P-T conditions used for aqueous geochemical calculations. White horizontal boxes show the effective $^{40}Ar/^{39}Ar$ cooling ages of amphibole (Am, Growdon et al., 2013) and muscovite (Ms, this study) in the Wepawaug Schist. Vertical white boxes show the times and PT conditions of recrystallized fabric-forming (white) and pseudomorphic (confetti filled) muscovite. For other explanation refer to text. Abbr. as in figure 2.

3.1. Sample strategy, structural and mineral nomenclature

The shear zone was mapped in the Bridgeport, Milford, Ansonia, and Mount Carmel quadrangles (Wathen, 2020; Wathen et al., 2015; fig. 2). Exposure is moderate but becomes excellent in across-strike stream cuts in the Ansonia and Milford quadrangles. One hundred thin sections cut perpendicular to both the dominant foliation and to local crenulations were studied using optical and electron petrography. Those samples showing the most diverse microstructures were selected for detailed study. We refer to the dominant foliation in any outcrop or thin section as 'Sn,' but because of the complicated overprinting cleavages, the dominant foliations (Sn) among these samples have demonstrably different ages. Older and younger foliations with relative ages established by cross cutting relationships within an outcrop or thin section are identified as Sn-1, Sn+1, and so on. To avoid clutter and to minimize concealing important microstructures only a subset of microstructures displayed in the figures below are highlighted with colored symbols; details of other features can be identified by enlarging the digital images. Metasomatic replacement reactions written below are balanced with Fe end-member formulae (given in Holland & Powell, 2011). This simplifies the reactions and allows activity diagrams to be calculated with SUPCRTBL (Zimmer et al., 2016). Abbreviations follow Spear (1995) and Holland and Powell (2011) except where longer abbreviations would mask the microstructures being described. These include C for chlorite, Q for quartz, and T for tourmaline.

3.2. Electron beam analysis

Most electron microprobe analyses (EMPA) and all element maps and backscattered electron (BSE) images were generated in the U.S. Geological Survey, Reston Microbeam Laboratory on a fully automated JEOL 8900 Electron Microprobe with five wavelength dispersive analyzers. Supporting electron microprobe analyses of sample WP-29 were made on a Cameca SX50 at Indiana University (Wathen, 2020). Details of methods including results are given in Supplementary

information (text, tables S1–S7, figs S1–S5) and in Wintsch et al. (2024). Na element maps show the distribution of muscovite blades with contrasting Na contents at the scale of the grains. EMPA analyses provide quantitative context for the color intensity variations present on these maps.

3.3. Argon isotopic analysis

Sample preparation for argon isotopic analysis of muscovite involved two separation methods: standard bulk rock muscovite separation (McWilliams et al., 2013) and a microscope-mounted micro-drill to isolate selected microstructures in phyllonites (Supplementary information; Wathen, 2020). These separates were irradiated for 30 MWH in the central thimble of the USGS-TRIGA facility in two irradiations in 2014 (KD61) and 2017 (KD65). Age plateaus are defined as consisting of three or more contiguous steps that contain > 60% of the $^{39}Ar_K$ and the probability-of-fit of the weighted-mean age of those steps is greater than 5% (Ludwig, 2012). Details of the analytical methods and constants used during data reduction are given in Supplementary information (text and table S8) and in Wintsch et al. (2024).

3.4. One-dimensional thermal modeling: P-T-time path

To establish a pressure-temperature-time (PTt) path for the rocks of the EDsz that is geodynamically plausible, we model this path to comply with the metamorphism of the protolith, the Wepawaug Schist. We employ the 1-dimensional thermal models of England and Thompson (1984) and Haugerud (1989) for conductive heating produced by crustal loading and unloading. Values of crustal properties given in Wintsch et al. (1992) in eastern Connecticut are appropriate for western Connecticut because peri-Gondwanan lower crust has been identified there as well (Sevigny & Hanson, 1993). The model PTt path was constrained to capture (1) the thermobarometric estimates in P-T space from both metamorphic petrology (Ague, 1994b, 2002) and from fluid inclusion data (Dabrowski & Evans, 2009; fig. 3), (2) the geochronologic and thermochronologic data in T-t space (see sec. 2.0), (3) the age of deposition of the original sediment (~410 Ma, by correlation with The Straits Schist, Wintsch et al., 2017), and (4) the non-conformity with Upper Triassic sediments on the western margin of the Hartford basin (Wheeler, 1937). The path was calculated iteratively by adjusting the times, rates, and durations of loading and unloading events until all these data were captured. Loading and unloading rates of 3, and 3 and 9 mm/yr., respectively (fig. 3B) captures these constraints. It also captures the ~100 m.y. dwell-time at lower greenschist facies conditions required by the muscovite $^{40}Ar/^{39}Ar$ data in the EDsz (sec. 5.2). Trial calculations show that the choice of values for geophysical variables given in Wintsch et al. (1992) does not significantly affect the position or the shape of the PTt path calculated.

3.5. Thermodynamic calculations

3.5.1. PSEUDOSECTIONS

Phase equilibrium (pseudosection) modeling was performed using Perple_X (Connolly, 2005, 2009) and the thermodynamic database (DS622) of Holland and Powell (2011) in the MnNCKFMASHTi system with H_2O in excess over the *P-T* range of 0 to 1.2 GPa and 300-700 °C (fig. 3A). Details of the calculations and bulk rock compositions for average chlorite-biotite grade and kyanite grade compositions of the Wepawaug Schist from Ague (1994a) are reported in Supplementary information. We adopt the pseudosection calculated from the average composition of chlorite-grade rocks (figs. S4, S5) because it better predicts the mineral compositions and assemblages present in the Wepawaug Schist at higher grades.

3.5.2. AQUEOUS GEOCHEMISTRY

To elucidate the role of aqueous fluids that facilitate reaction and pressure solution we employ SUPCRTBL (Zimmer et al., 2016) to calculate aqueous activity diagrams using equilibrium constants for the replacement reactions presented below. Aqueous activity diagrams have an advantage over pseudosections in that they show the effect of temperature and pressure on the *size* of the stability field of each mineral in chemical potential space. A limitation of SUPCRTBL is that it cannot calculate the compositions of aqueous fluids in equilibrium with complex solid solutions. We opt for the Fe end-member system because it is more germane to the Fe-rich minerals of these rocks (staurolite, garnet, Ague, 1994b; chlorite, this study). However, calculations of both the pseudosection and the activity diagrams are derived from the same thermodynamic database for solid phases (version DS622, Holland & Powell, 2011) and are thus consistent regarding solid end-member data. The consequence of choosing the Mg-free system on the activity diagrams calculated is to reduce the size of the biotite and chlorite stability fields. However, neither the topology of the diagrams nor the conclusions reached in this contribution are affected by this simplification.

4. RESULTS

4.1. Metamorphic history: establishing a PTt path

The pressure-temperature (PT) diagram of figure 3 provides a metamorphic context for the development of the microstructures in the phyllonites described below. Key data from this pseudosection (see Supplementary information) included on this figure are the biotite, garnet, and staurolite isograds (dashed red lines) and contours of the paragonite component (pg) of muscovite (solid and dashed green lines). These calculations predict a maximum of 36 mol % pg at ~600 ºC and ~0.5 GPa, dropping to < 10 mol % pg at greenschist facies conditions (fig. 3A) making the pg content of muscovite a good monitor of the metamorphic conditions of muscovite crystallization. Added to this PT diagram (fig. 3B) are the results of 1-dimensional thermal

modeling of the PTt path (section 3.4) of the Wepawaug Schist (bold dashed black line).

4.2. Structural relationships

Rocks of the EDsz are dominated by phyllites and phyllonites of pelitic composition that contain small (> cm thick) concordant quartz ribbons and beards (figs. 4–8, S3, S4; Wathen, 2020; Wathen et al., 2015). Foliation is very well developed but mineral lineations on phyllonitic surfaces are absent. Rather, multiple overprinting foliations dominate most foliation surfaces. Almost all structures at the outcrop scale are ductile, but brittle faults with slicken lines are present in some outcrops; these can never be traced beyond a single outcrop.

The Wepawaug Schist marks the eastern boundary of the shear zone. The contacts between the lower greenschist facies phyllonites and the host schists are sharp but the rocks are locally interlayered. For example, muscovite ± chlorite bearing foliations cut and replace amphibolite facies muscovite + biotite schists on the scale of mm, while adjacent biotite and garnet are incompletely replaced by chlorite (fig. 5A, B). In the same sample at least four foliations dominated by muscovite truncate earlier muscovite + biotite foliations (fig. 5C–F). In fact, multiply overprinting foliations are characteristic of the phyllonites in general (figs. 4–11). Porphyroblasts of garnet, staurolite, kyanite, and intermediate plagioclase that survive exhumation in the Wepawaug Schist (Ague, 1994b; T. H. Bell & Newman, 2006; Growdon et al., 2013; Wathen, 2020) become progressively replaced by randomly oriented muscovite or chlorite near the shear zone (figs. 4–8, S4); this replacement is complete in the interior of the shear zone (e.g., fig. 4).

Pelitic schist and orthogneiss mark the western boundary of the shear zone. There the schist becomes pinstriped and orthogneisses are strongly foliated, locally becoming mylonitic schist (Wathen et al., 2015). Phyllonites approaching the western boundary include tectonic slivers of Wepawaug Schist, muscovite-quartz granofels, quartzite, and amphibolite, especially in the southern Ansonia quadrangle (Fritts, 1965). The progressive replacement of porphyroblasts and the occurrence of tectonic slivers of Wepawaug Schist within the phyllonite provide evidence that the phyllonites are derived from the Wepawaug Schist.

4.3. Microchemical results

The compositions of all rock-forming minerals in the Wepawaug Schist are available (Ague, 1994b, 2002; Growdon et al., 2013). The compositions of minerals in the EDsz are given in table S5 and Wintsch et al. (2024), and generally overlap with those in the Wepawaug Schist (Ague, 1994b). To preserve microstructural context, the locations of EMPA analyses are plotted on optical and backscattered electron images of the minerals (figs. 4G, 6B–E, 8A, C, D, 10, S3, S4), and their numbers are keyed to the analysis number in table S5. The suite of muscovite analyses shows a continuous compositional variation in pg content, from >35% to < 5% (fig. 6E, F; fig. S1). This range records compositions reflecting near maximum P-T conditions of the Wepawaug Schist to the lower greenschist facies of the EDsz (green contours, fig. 3). The compositions of chlorite are all Fe-rich ripidolite, analyses across single chlorite grains or clusters of grains show no strong zoning at the scale of our analyses (fig. S2).

4.4. Petrography

Mineral reactions in the phyllonites and adjacent wall rocks occur in two settings. One is pseudomorphic replacement of high-grade minerals by low-grade minerals. The other is the replacement of earlier minerals by minerals that define new cleavages. They are discussed in this order below.

4.4.1. STATIC REPLACEMENT REACTIONS

Staurolite replaced by muscovite. – Staurolite porphyroblasts up to 1 cm long occur in the high-grade Wepawaug Schist where they are surrounded by foliations defined by muscovite + biotite (T. H. Bell & Newman, 2006). However, within the EDsz the staurolite porphyroblasts are completely replaced by muscovite of two grain sizes (figs. 4G, S4). The larger of the two contains slightly more Na and less Fe – Mg than the finer grains (Supplementary information) but all contain < 0.15% pg (figs. 4G, 6F). These small grains also contain more Al and less Si than fabric-forming muscovite (fig. 6G). This replacement can be described by reaction 1 (table 1) that requires the introduction of both H_2O and H^+. Quartz is not present within the pseudomorphs (e.g., fig. 4) which supports the operation of reaction 1 that consumes SiO_2. As written the reaction involves a large increase in volume, but if the reactant SiO_2 is treated as quartz (inclusions are common in staurolite, Newman, 2001) the volume increase is much less (table 1).

Garnet replaced by chlorite. – Garnet (X_{alm} = 0.65–0.80, Ague, 1994b) is common in the higher-grade Wepawaug Schist (T. H. Bell & Newman, 2006). On the margins of the EDsz garnet is partially replaced by chlorite (figs. 5A, B, 6A; 8A), but within the shear zone garnet is completely replaced by randomly oriented chlorite flakes (e.g. fig. 4B, C, lower left). The compatibility of chlorite with muscovite (small flakes with chlorite, fig. 5B) indicates that the replacement occurred under lower greenschist facies conditions. The reaction describing this replacement (no. 2, table 1) requires the introduction of H_2O and releases H^+. It also predicts a significant volume increase, but this increase drops to +25% using the compositions of ripidolite analyzed here.

Biotite replaced by chlorite. – Some relic grains of biotite are partially or completely replaced by chlorite. Petrographic evidence for this replacement is found in grains where the replacement is incomplete, preserving the shape of the original biotite grain (figs. 5A, B, 7E, F, 8A). This pseudomorphic replacement involves a small loss in volume (reaction 3, table 1) especially if quartz precipitates locally.

Plagioclase replaced by albite. – Plagioclase is present in the Wepawaug Schist with intermediate compositions from ~An_{10} to ~An_{40} in pelitic rocks (Ague, 1994b). However, plagioclase grains in muscovite + chlorite phyllonites have An

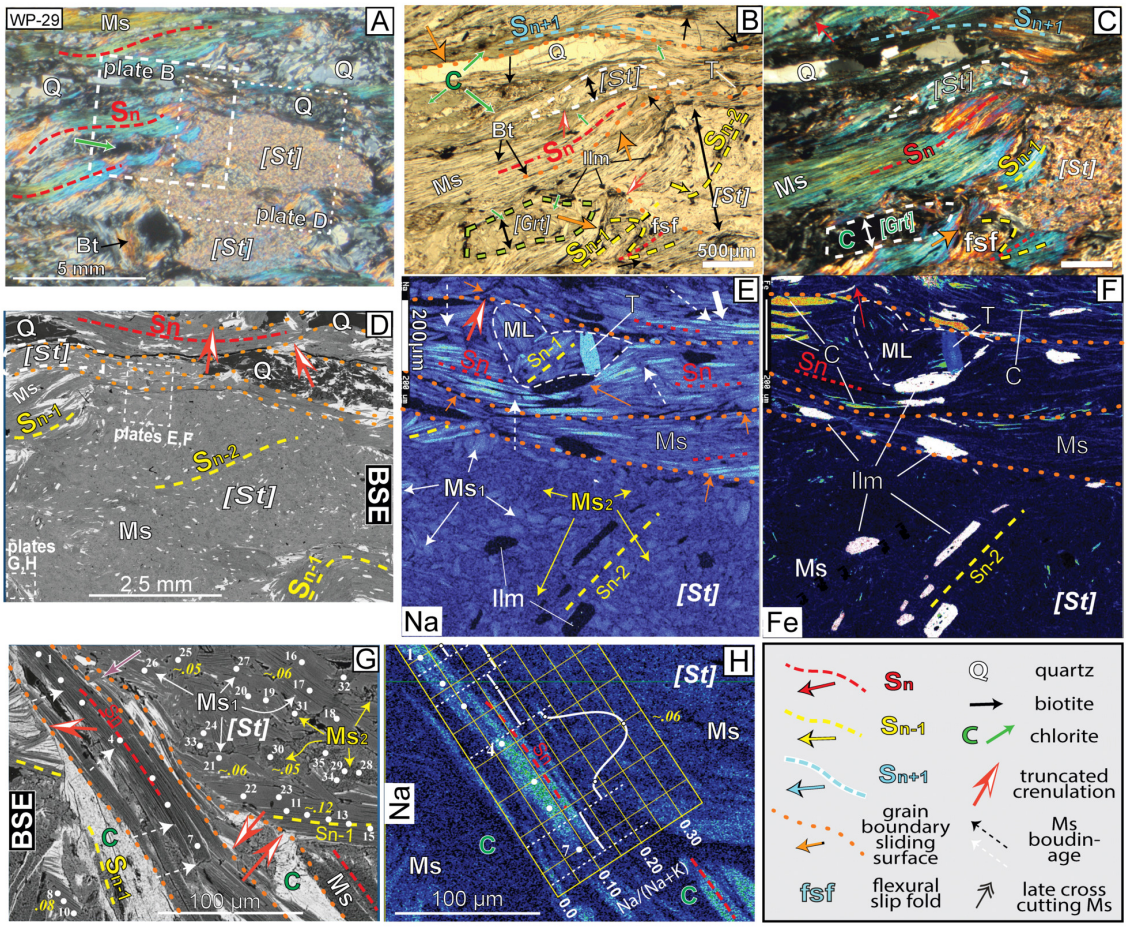

Figure 4. Images of textures and microstructures from sample WP-29 (refer also to fig. S4) on the eastern margin of the EDsz. The legend explains the symbols here and in figures below. (A) Crossed polarized light CPL) image of the dominant muscovite + biotite (Bt, black arrows) foliation (Sn) interlayered with quartz (Q) ribbons and hosting a muscovite (Ms) pseudomorph after staurolite (*[St]*, grainy orange pattern). Dashed and dotted boxes show the locations of plates B and D. (B) and (C) Plain polarized light (PPL) and CPL images of pseudomorphs (bi-directional black arrows) within Sn defined by muscovite > biotite. Weakly deformed (right) and flattened (dashed white outline) pseudomorphs of muscovite after staurolite, and a moderately flattened pseudomorph of chlorite after garnet (dashed green outline, *[Grt]*) are indicated. Foliation Sn-2 is defined by trails of ilmenite (Ilm) inclusions in the staurolite pseudomorph; Sn-2 is folded against the former staurolite porphyroblast producing Sn-1. Sn with a parallel quartz (Q) ribbon wraps around the larger pseudomorph. Some of many grain boundary sliding (GBS) surfaces are marked by dotted orange lines. Red-white arrows point to truncated crenulations. (D) BSE of quartz-free muscovite (gray) pseudomorph after staurolite showing ilmenite inclusions (small white bars) defining Sn-2 foliation. Sn-1 and Sn matrix foliations are indicated. (E) A Na element map showing two grain sizes of muscovite (Ms_1 and Ms_2) in the pseudomorph after staurolite in contact with external foliation composed of muscovite flakes of Na-rich (sky blue) and Na-poor (dark blue) compositions. A microlithon (ML) containing Sn-1 and a tourmaline (T) grain is outlined with a dashed white line. GBS surfaces show muscovite folia truncating muscovite (reaction 7, table 1) and dashed white arrows identify boudinaged grains. (F) An Fe element map of the area in plate E, showing the distribution of ilmenite, and the very limited participation of chlorite in Sn. (G) A BSE image (location in plate D) showing the textures and distribution of muscovite and chlorite on the margin of a staurolite pseudomorphed by two grain sizes of muscovite. Numbered white dots show the locations of EMPA analyses, and yellow numbers in italics indicate the average molar % pg in muscovite (Wintsch et al., 2024). A large relic pg-rich muscovite grain (left) that defines Sn truncates earlier crenulated (Sn-1) chlorite-bearing foliations (red-white arrows). The pg-poor muscovite in the pseudomorph cuts Sn (violet arrow, upper left). White dashed arrows mark steps in Na content identified in plate H. (H) A Na element map showing the distribution of Na in muscovite in grains shown in plate G. The pg composition (graphed) of the 200 µm long muscovite flake that defines Sn is stepped with dotted white lines marking the boundaries between compositional zones.

Table 1. Balanced reactions describing replacement of metamorphic minerals.

No.	Abbr.	Balanced reaction [1]	$\Delta V_{(solid)}\%$ [2]	$\Delta V_{(solid)}\%$ [3]
		Static Replacement Reactions		
(1)	St = Ms	$1\ Fe_4Al_{18}S_{7.5}O_{44}(OH)_4 + 10.5\ SiO_{2(aq)} + 6\ K^+ + 2\ H^+ + 3\ H_2O = 6\ KAl_3Si_3O_{10}(OH)_2 + 4\ Fe^{2+}$	+88	+23
(2)	Grt = Chl	$1\ Fe_3Al_2Si_3O_{12} + 2\ Fe^{2+} + 6\ H_2O = 1\ Fe_5Al_2Si_3O_{10}(OH)_8 + 4\ H^+$	+85	
(3)	Bt = Chl	$2\ KFe_3AlSi_3O_{10}(OH)_2 + 4\ H^+ = 1\ Fe_5Al_2Si_3O_{10}(OH)_8 + 1\ Fe^{2+} + 2\ K^+ + 3\ SiO_{2(aq)}$	-31	-9
(4)	Pl = Ab	$0.93\ Na_{.85}Ca_{.15}Al_{1.15}Si_{2.85}O_8 + 0.14\ Na^+ + 0.28\ SiO_{2(aq)} = Na_{.93}Ca_{.07}Al_{1.07}Si_{2.93}O_8 + 0.07\ Ca^{+++9}$	+ 9	+0.5
		Cleavage-Forming Reactions		
(5)	Bt = Ms	$3\ KFe_3AlSi_3O_{10}(OH)_2 + 20\ H^+ = 1\ KAl_3Si_3O_{10}(OH)_2 + 9\ Fe^{2+} + 2\ K^+ + 6\ SiO_{2(aq)} + 12\ H_2O$	-70	-40
(6)	Chl = Ms	$3\ Fe_5Al_2Si_3O_{10}(OH)_8 + 2K^+ + 28\ H^+ = 2\ KAl_3Si_3O_{10}(OH)_2 + 3\ SiO_{2(aq)} + 15\ Fe^{++} + 24\ H_2O$	-56	-45
(7)	Ms = Ms	$2.8\ K_{0.7}Na_{0.3}Al_3Si_3O_{10}(OH)_2 + 0.74K^+ + 0.9Fe^{++} + 0.6SiO_{2(aq)} + 1.2H_2O = 3\ K_{0.9}Na_{0.1}Fe_{0.3}Al_{2.8}Si_3O_{10}(OH)_2 + 0.54Na^+ + 2\ H^+$	+7	+3.6

1. Reactions balanced on Al (Carmichael, 1969) with formulae given in Holland and Powell (2011).
2. $\Delta V_{(solid)}$ calculated without aqueous species, consistent with petrography.
3. $\Delta V_{(solid)}$ calculated with SiO_2 volume as quartz.

compositions of An_{02}-An_{08} (e.g., figs. 10, S3, S4). Where relic plagioclase is present, grains are partially replaced by albite (aqua and dark blue, Ca element map, fig. 7D). Using generalized compositions of plagioclase analyzed in these rocks, the reaction involves a small volume increase unless SiO_2 is treated as quartz (no. 4, table 1). The reaction consumes SiO_2, which may account for the lack of quartz in these muscovite + albite folia.

4.4.2. CLEAVAGE-FORMING REACTIONS

Biotite replaced by muscovite. – Biotite is ubiquitous in the Wepawaug Schist of appropriate metamorphic grade where it helps define Acadian foliations (Newman, 2001; e.g., figs. 4, 5, 6A, E). Small grains of biotite persist in many phyllonite samples, but muscovite flakes defining Sn truncate biotite grains leaving wedges and slivers of biotite between new blades of muscovite (figs. 4B, 5, 6A). In the Na element map of figure 5D four generations of muscovite cleavages cut earlier muscovite + biotite fabrics, with Na-rich grains appearing yellow, and muscovite in progressively younger folia displaying decreasing Na content consistent with falling metamorphic temperatures. The truncation of biotite by muscovite grains is described by reaction 5 (table 1). This replacement involves a large volume decrease and requires the introduction of reactant H^+, so the reaction could be driven by a high normal stress and by an increase in the acidity of the grain boundary film.

Chlorite replaced by muscovite. – In some samples foliations containing muscovite + chlorite are truncated by foliations containing nearly pure muscovite folia (figs. 6B, 9, 10, S3). The replacement of chlorite by muscovite (reaction 6, table 1) involves a large volume decrease and requires the introduction of H^+. Thus, increases in normal stress and in acidity would drive the reaction toward muscovite.

Muscovite replacement by muscovite. – The most important reaction producing foliations is the replacement of muscovite in earlier foliations by muscovite in crosscutting foliations. Evidence for this reaction comes from the pervasive truncations of the muscovite grains in the older microstructures by muscovite in cross cutting folia, commonly along GBS surfaces. Such truncations can be recognized optically (figs. 4–8) but are more easily identified in BSE images and element maps (figs. 4–11). For example, in sample WP-29 splinter-shaped Na-rich muscovite grains (pale blue, fig. 4E) are sheathed and locally truncated by folia of Na-poor muscovite grains (dark blue). Reaction 7 (table 1) describes this replacement in which quartz is a reactant. The absence of quartz in the new Na-poor muscovite folia (refer to most figures) is consistent with its consumption. Less common are folia defined by Na-rich muscovite truncating folia containing Na-poor muscovite. Sample WP-29 (fig. 4G, H, S4B) shows that folia containing relic Acadian muscovite (pg up to 30%) cut both earlier muscovite folia and muscovite in pseudomorphs after staurolite. In this case, the relic Na-rich muscovite survived in the Sn foliation despite its chemical metastability.

Also common in more thoroughly recrystallized samples are foliations containing Na-poor muscovite truncated by foliations with similarly Na-poor muscovite. In sample WP-45 all the muscovite analyzed contains < 12% pg (figs. 9, 10). However, the concentrations of pg in muscovite in three successive foliations falls from ~11 to ~7% (fig. 10B). The falling pg content follows a trend of increasing muscovite mode in the host foliations. This demonstrates dissolution, recrystallization, and metamorphic differentiation in these overprinting cleavages.

Evidence for muscovite recrystallization is also found in the hinges of folds. For example, the overturned limbs of the kink bands in sample WP-02 have gained both K

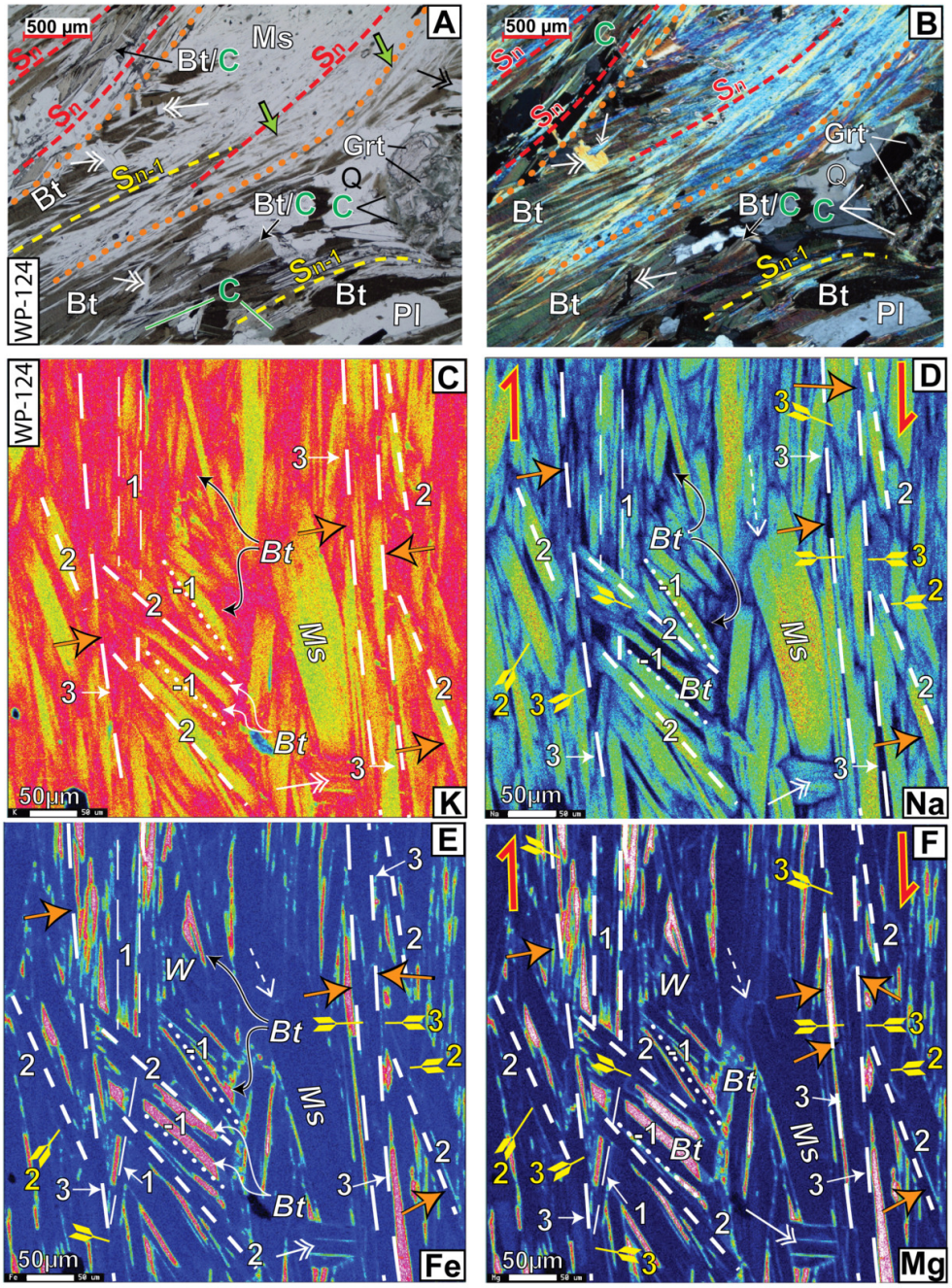

Figure 5. Optical and element map images of sample WP-124 (refer also to fig. 7E, F). (A), (B) PPL and CPL images of muscovite + chlorite ± biotite Sn folia (blue birefringence, plate B) cutting and replacing muscovite + biotite ± plagioclase folia in Sn-1. Biotite (Bt/C) and a fractured garnet porphyroblast (Grt, right) are partially pseudomorphed by chlorite with small flakes of muscovite. (B). Late muscovite (double headed arrows) cut across all grains. (C) A K element map showing that Na-rich muscovite flakes (yellow) are distributed in several overprinting folia (-1, 1, 2, 3, dotted through long dashed lines) and that Na-poor muscovite and biotite have similar K concentrations (red). (D) A Na element map of region C showing that the Na content of muscovite falls following yellow to green to blue in succeeding younger folia. Feathered arrows point to Fe-Mg-bearing muscovite flakes in S2 and S3. (E) Fe element map in which red through green blades are biotite. Dark blue regions contain Na-rich muscovite, whereas pale blue bands reflect Fe-bearing muscovite. Biotite occurs as interstitial wedges (W) between muscovite folia. (F) Mg element map showing biotite (warm colors), Na-rich muscovite (dark blue), Mg-bearing muscovite (pale blue), and the right lateral slip direction (red arrows).

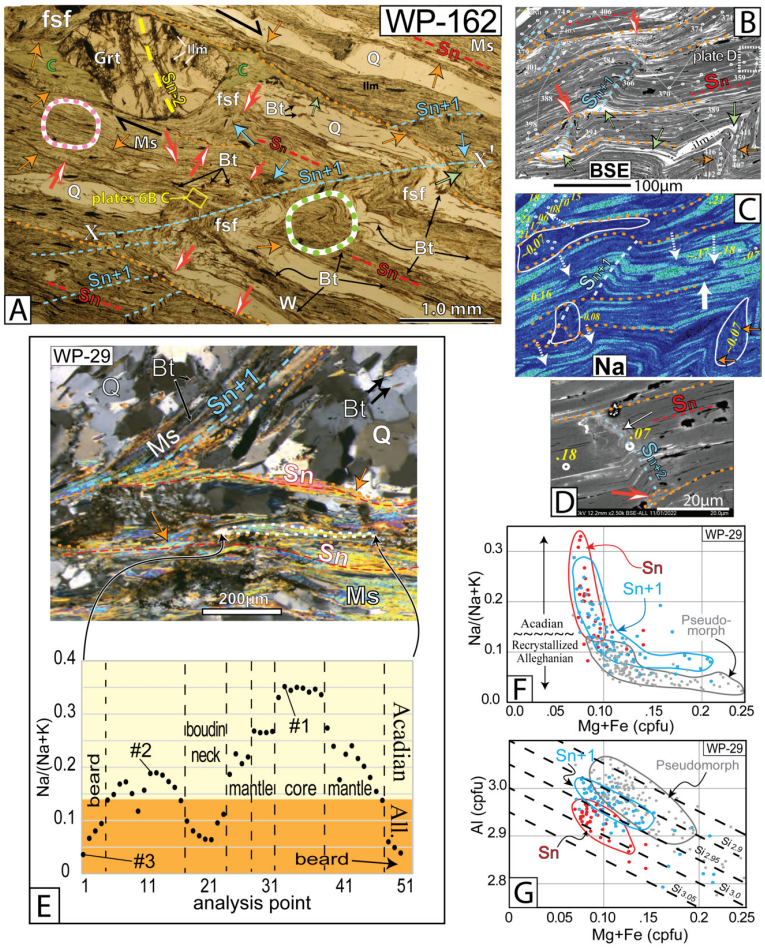

Figure 6. (A). PPL image of sample WP-162 showing muscovite + biotite Sn interlayered with quartz ribbons crenulated by Sn+1 (dashed blue lines and arrows). Blades of amphibolite facies (fig. S4) ilmenite inclusions (black) in garnet preserve an Sn-2 foliation and chlorite occurs in sigma-shaped strain shadows. Crenulations in the center, and around the garnet formed by fsf with amplitudes dying out against GBS surfaces (orange dotted lines) where muscovite replaces muscovite. The pink and green dotted circles identify areas like those dated by $^{40}Ar/^{39}Ar$ methods (refer to text; fig. 8). The asymmetry of folds and chlorite beards indicate a dextral sense of shear (black barbed arrows). (B) A backscattered electron image (yellow box, plate A) showing the truncation by dissolution of Sn along GBS surfaces and the crenulation of Sn muscovite by Sn+1. The darker gray muscovite reflects a higher pg content (refer to panel C). Some sliding surfaces (orange dotted lines) and fold hinges are filled with chlorite (white, green arrows). Thin white lines joining white dots show the locations of EMPA points with numbers keyed to analyses in table S5. Scale bar below for plates B and C. (C) Na element map of image B showing the distribution of Na-rich muscovite (pale blue, yellow numbers give pg mole %); some are boudinaged (dashed arrows) with necks filled by Na-poor muscovite. Regions of tight overturned kink folds (white circles) contain Na-poor muscovite. (D) An enlargement from plate B (dotted box) showing Sn crenulated by very late cleavage (Sn+2, dotted blue line). EMPA spots (white circles) show that the region of the fold hinge (paler gray, white arrow) is recrystallized to a low pg content relative to the limbs of the fold (7% vs. 18%). The core of the fold is intensely crenulated (red/white arrow). (E) A CPL image showing Sn defined by muscovite with biotite truncated by Sn+1. The dotted white line outlines the muscovite grain analyzed by EMPA; black arrows show the start and end point of the analytical traverse. The lower graph shows steps in the mole % pg in this boudinaged grain, where dashed vertical black lines identify these steps. Compositions range from 0.35% at its interior core to <7% in the beards and boudin neck (#1 to #3 refer to EMPA analyses in appendix A, table 6A). (F) A plot of muscovite analyses from sample WP-29 showing pg % vs Fe+Mg cpfu (based on 11 O) in grains in Sn, Sn+1, and in muscovite pseudomorphs after staurolite (e.g., fig. 4). Wavy line at ~12% pg shows approximate boundary between muscovite crystallized during the Acadian and retrograde muscovite crystallized during the Alleghanian. (G) A plot of the muscovite analyses from plate F showing octahedral Al vs. Mg + Fe. Black dashed lines contour Si (cpfu).

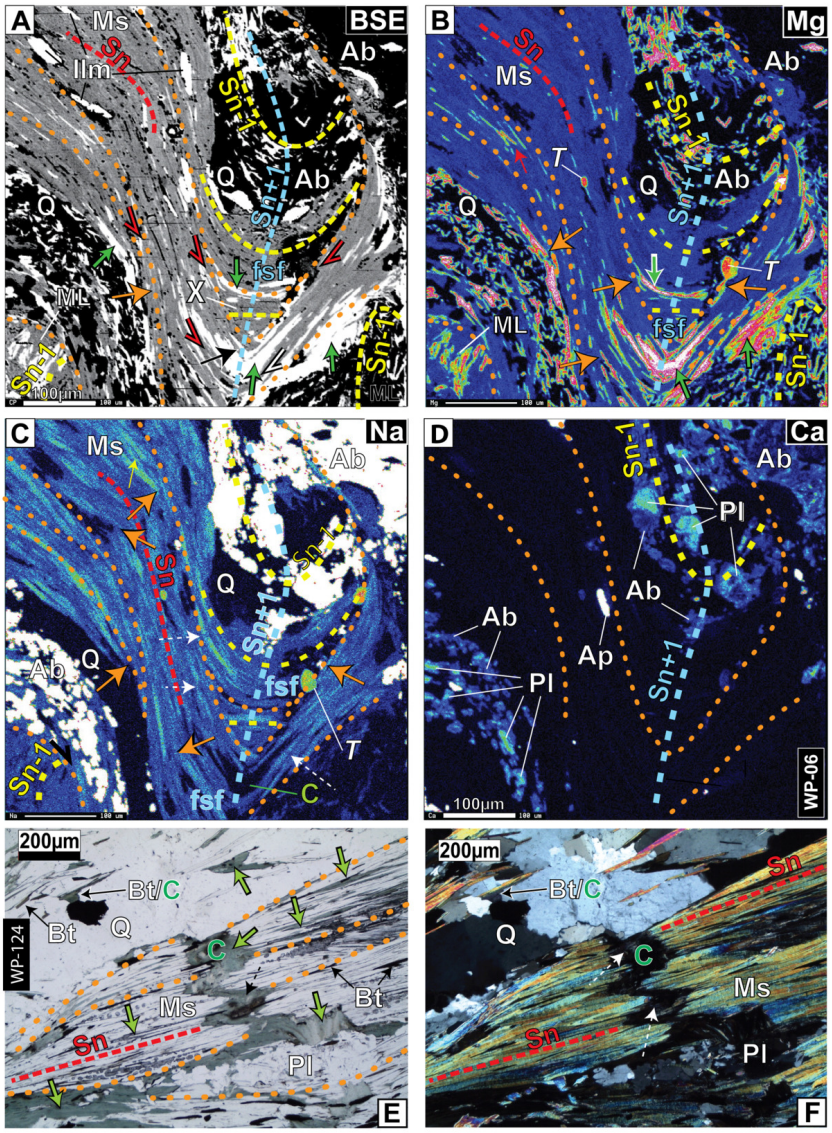

Figure 7. (A–D) A set of images of folded composite muscovite folia (sample WP-06). GBS surfaces show the reaction of muscovite muscovite (no. 7, table 1). 100 µm scale bar applies to all. (A) BSE image of folded Sn folia defined by muscovite (Ms, gray) with chlorite (C, green arrows) and ilmenite (Ilm, white laths). Sn-1 preserved in microlithons (ML). Quartz and plagioclase appear black. GBS surfaces are sub-parallel to Sn. Red barbs indicate slip direction in flexure-slip fold (fsf). (B) Mg element map showing that chlorite (in colors of green, orange, red, and white) is absent from fold limb, but is localized in Sn-1 and as crescent-shaped grains in the hinges of flexural slip folds (fsf). Tourmaline grains (T) are present in fold limbs. (C) Na element map showing that Na-rich muscovite grains (aqua) are entrained in the dominant foliation Sn but are truncated and/or boudinaged along dissolution and GBS surfaces. These are in a matrix of younger Na-poor muscovite grains that define Sn. Plagioclase (Pl) is white, and quartz is black. (D) Ca element map showing the distribution of relic intermediate plagioclase partially replaced by albite. Apatite grain (Ap) is white. (E) PPL image of sample WP-124 showing a muscovite + biotite composite foliation (Sn) between a quartz ribbon above and a cluster of plagioclase grains below. Sn contains multiple GBS surfaces and is boudinaged with the zig-zag shaped boudin neck filled with randomly oriented, coarse chlorite flakes. Biotite in the quartz ribbon is partially pseudomorphed by chlorite. (F) CPL image of E showing the boudin neck, the random orientation of plagioclase grains, and the weakly sutured boundaries between quartz grains.

(brighter red in fig.11A) and Mg (fig. 11C, F) and lost Na (darker blue in fig. 11B, E). This recrystallization is more complete in the complicated flexural slip folds (identified in fig. 11B by 'fsf'). The fold hinges are especially thoroughly recrystallized (fig. 11D–F). Figure11D shows the hinge is made up of only muscovite (bright red) whereas in figure 11E selected grains are more completely recrystallized, losing Na and gaining Mg (fig. 11E, F). Muscovite flakes in the kink bands of sample WP-162 are also recrystallized at the scale of a few µm (fig. 6D).

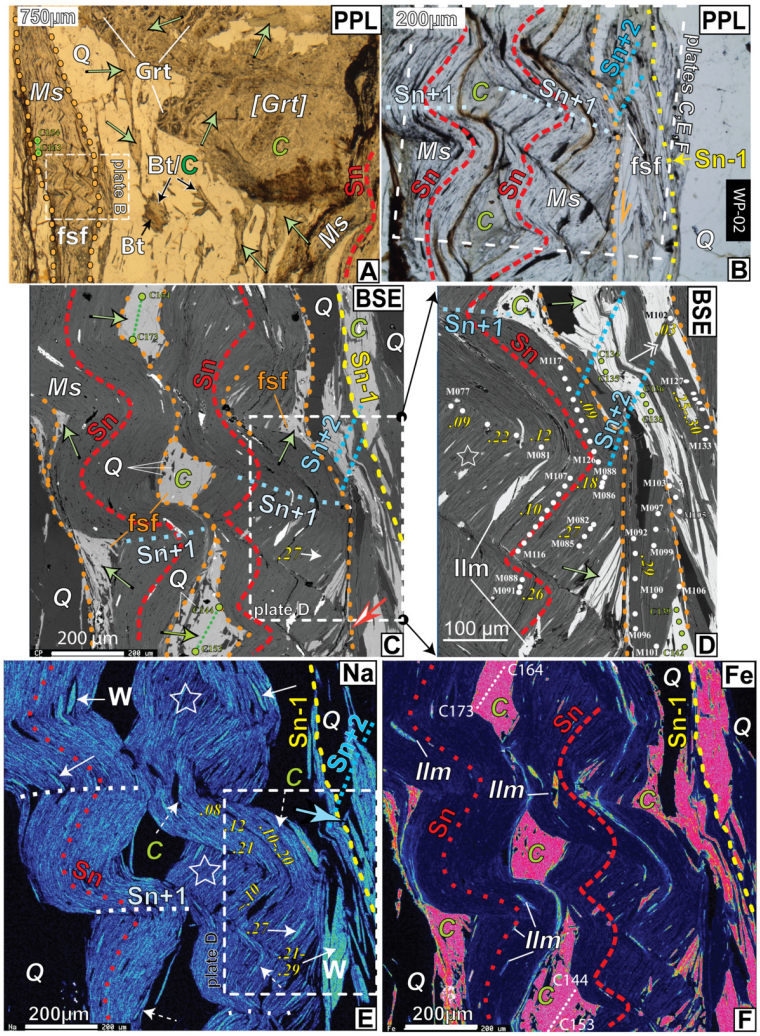

Figure 8. Images of sample WP-02. White and green dots numbered M077 etc. and C134 etc. in plates A, C, and D refer to muscovite and chlorite analyses given in Supplementary information. Truncations along GBS surfaces show dissolution of chlorite and muscovite, and precipitation of new muscovite (reactions 6, 7, table 1). (A) PPL photomicrograph of sample WP-02 showing a garnet porphyroblast *[Grt]* incompletely replaced by chlorite and enveloped in muscovite-rich folia and quartz ribbons. Relic garnet (high relief) and partial pseudomorphic replacement of biotite by chlorite (Bt/C) are indicated. A double fold train (fsf) defined by muscovite alone on left. Dashed line box indicates location of plate B. (B) PPL image of muscovite folia (Sn) crenulated by Sn+1. An earlier foliation, Sn-1 (dashed yellow line) is crenulated by Sn+2 (dashed dark blue line). Chlorite (C) fills fold hinge regions. Dashed line box indicates location of plates C, E, F. (C) A backscattered electron image of most of the region of plate B showing two Sn muscovite folia crenulated by Sn+1 and sandwiched between quartz ribbons and separated by GBS surfaces. Sn+2 crenulates Sn-1 (right side of the image). Folia are composed of almost pure muscovite and hinges are filled with coarse-grained chlorite with minor quartz (Q). (D) An BSE enlargement of the boxed region in plate C showing detail of crenulated Sn, with chlorite filling fold hinges. Analytical spots 127-133 shows minimal zoning in Na-rich muscovite flake (pg 25–30%). Rare muscovite flake subparallel to Sn+2 axial plane cutting chlorite in Sn-1(double-headed arrow) contains 0.03 % pg (e.g., EMPA spot M102 upper right). Yellow numbers in italics show % pg in adjacent EMPA spots. Medium gray grains in starred region shows overturned limb of crenulation is Na-poor. (E) A Na element map showing the intimate mixture of Na-rich blades and wedges (W) of Na-rich muscovite (pg > ~20%, pale blue) in a matrix of Na-poor (dark blue, pg <~12%) muscovite flakes. Na-rich muscovite folia define an Sn-1 foliation on the right side of the image. Dotted dark blue lines trace Sn + 2. Starred regions show the overturned limbs of crenulations are Na-poor. (F) An Fe element map showing the distribution of chlorite in extension sites (C, magenta) and small ilmenite blades (Ilm) within Sn folia. Note that chlorite participates in Sn-1 (yellow dashed line, right side of image) but is absent from Sn. Dotted white lines show EMPA traverses; numbers are keyed to EMPA data in Wintsch et al. (2024).

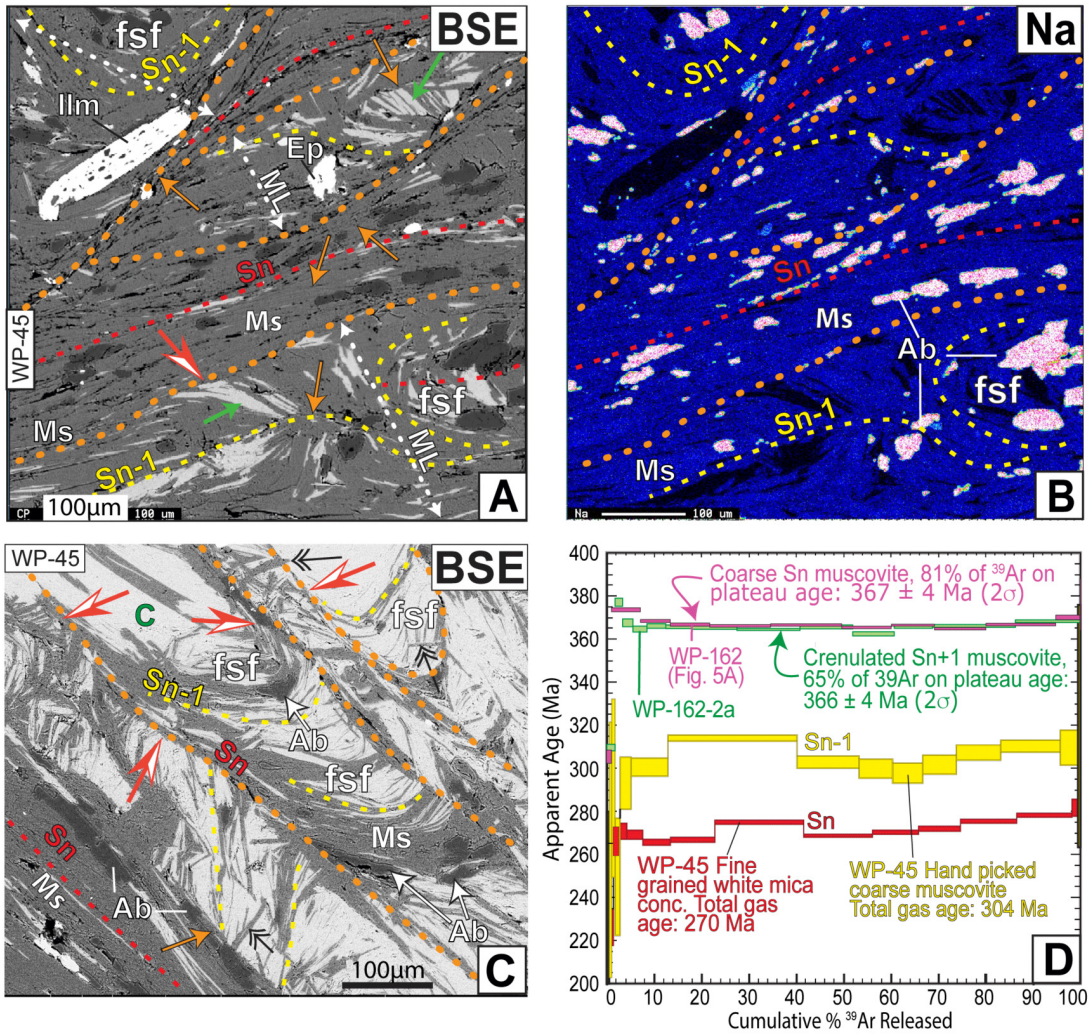

Figure 9. GBS surfaces truncate grains on both sides, showing the dissolution of chlorite and muscovite, and precipitation of new muscovite (reactions 6, 7, table 1). (A) BSE image from sample WP-45 showing Sn defined by muscovite (dark gray) with very minor chlorite. Sn folds Sn-1 (yellow dashed lines) creating microlithons (ML, white dashed bi-directional arrows) that contain coarse muscovite and interlayered chlorite. The microlithons are isolated by through-going GBS surfaces (dotted orange lines) and by smaller truncation surfaces (orange arrows). Dark gray laths are albite (Ab); ilmenite laths and epidote are labeled (Ilm, Ep). Disharmonic flexural slip folding identified by fsf. (B) Na element map of plate A showing the distribution blocky and lath-shaped grains of albite (pink) in Sn-1 and Sn, respectively. Muscovite is uniformly Na-poor (dark blue) showing complete replacement of Na-rich muscovite. (C) BSE image showing Sn defined by ~50 µm grains of muscovite (red dashed line) with rare chlorite crenulating Sn-1 (yellow dashed lines) that contains coarse-grained chlorite > muscovite; both (>~75µm). Less common small straight muscovite flakes (black arrows) cut muscovite and chlorite in both Sn and Sn-1. Disharmonic flexural slip folding identified by fsf. Red/white arrows point to crenulated grains in Sn-1. (D) $^{40}Ar/^{39}Ar$ age spectra from muscovite from Sn-1 (yellow bars) and from Sn (red bars). Two other muscovite $^{40}Ar/^{39}Ar$ age spectra from sample WP-162 are magenta and green corresponding to colors in figure 5A.

Chlorite filling extension sites. – Chlorite fills extension sites in deformed and crenulated foliations and around porphyroblasts. The latter site is common and involves chlorite forming beards in pressure shadows and boudin necks (figs. 6A, 7E, F, 10). Chlorite also commonly fills the gap between muscovite folia in fold hinges (green arrows, figs. 6A, B, 7A, B, 8).

4.5. Deformation mechanisms in the EDsz

4.5.1. PRESSURE SOLUTION

The reactions described above all involve dissolution, diffusive transport of aqueous species, and precipitation. Some reactions involve pseudomorphic replacement, but the cleavage-forming reactions define new microstructures.

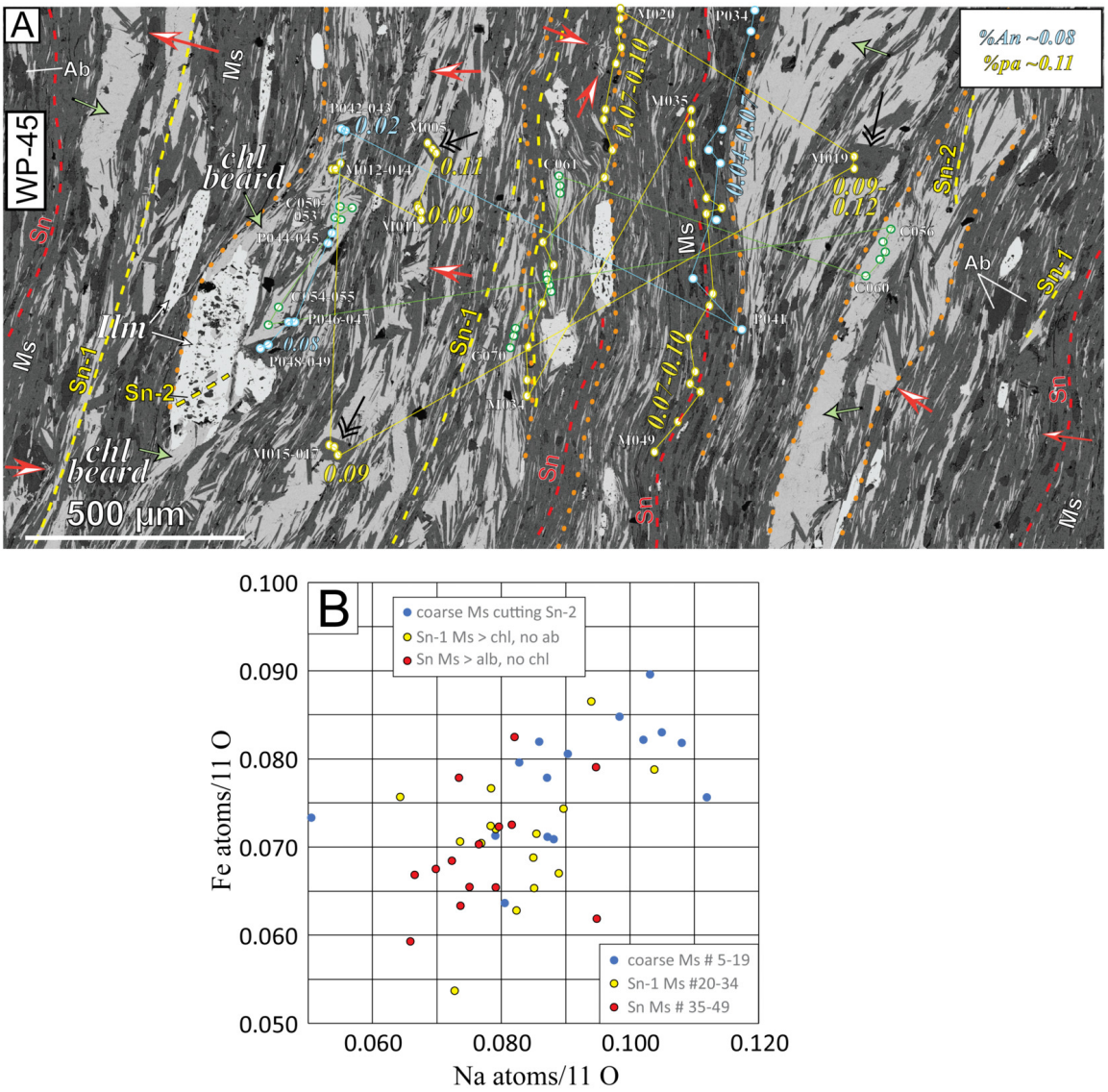

Figure 10. (A) BSE image of a portion from sample WP-45 (refer to fig. 9) showing Sn dominated by muscovite folia truncating and replacing muscovite in earlier folia (Sn-1, Sn-2). White numbers refer to analysis number (M, muscovite, P, plagioclase in Supplementary information); yellow and blue numbers in italics show the average pg and An contents of muscovite and plagioclase respectively in adjacent grains. GBS surfaces truncate muscovite and chlorite demonstrating dissolution and replacement by new muscovite in three generations of foliation. Note chlorite beards on large ilmenite (white) grain (left). (B) Graph comparing muscovite compositions in three microstructural sites. Relative to Sn, coarse muscovite grains (double headed arrows) have slightly more Fe and Na, Sn-1 contains less Na and Fe, whereas grains in Sn with albite and very little chlorite contain the lowest concentrations of Na and Fe.

The latter involve pressure solution that is more fully explored in section 5.4.

4.5.2. FRACTURING AND BOUDINAGE

Brittle features such as joints and small-scale faults are present in some outcrops; these likely reflect Mesozoic reactivation. Decimeter-scale cracking and boudinage in the field are rare except where ductility contrasts are high, such as broken quartzite layers in phyllonites (Wathen et al., 2015). At the grain scale, however, fracture of single muscovite grains or of packets of muscovite flakes in folia does occur. The coarsest grained example shows chlorite filling a boudin neck in a muscovite folium (fig. 7E, F). The parallel walls of the zigzag-shaped opening fit together, confirming a fracture-boudinage origin.

Fracture at the single grain scale also occurs. Na element maps identify single blades of Na-rich muscovite that have been boudinaged in their matrix of Na-poor muscovite (dashed white arrows, figs. 4E, G, H, 6C, E, 7C, 8E, 11B, E). They are recognized by the green to pale blue color of the Na-rich muscovite in the boudins and the dark blue color of the Na-poor muscovite filling the boudin necks. In general, the Na-rich boudinaged flakes contain > 15 % pg and the

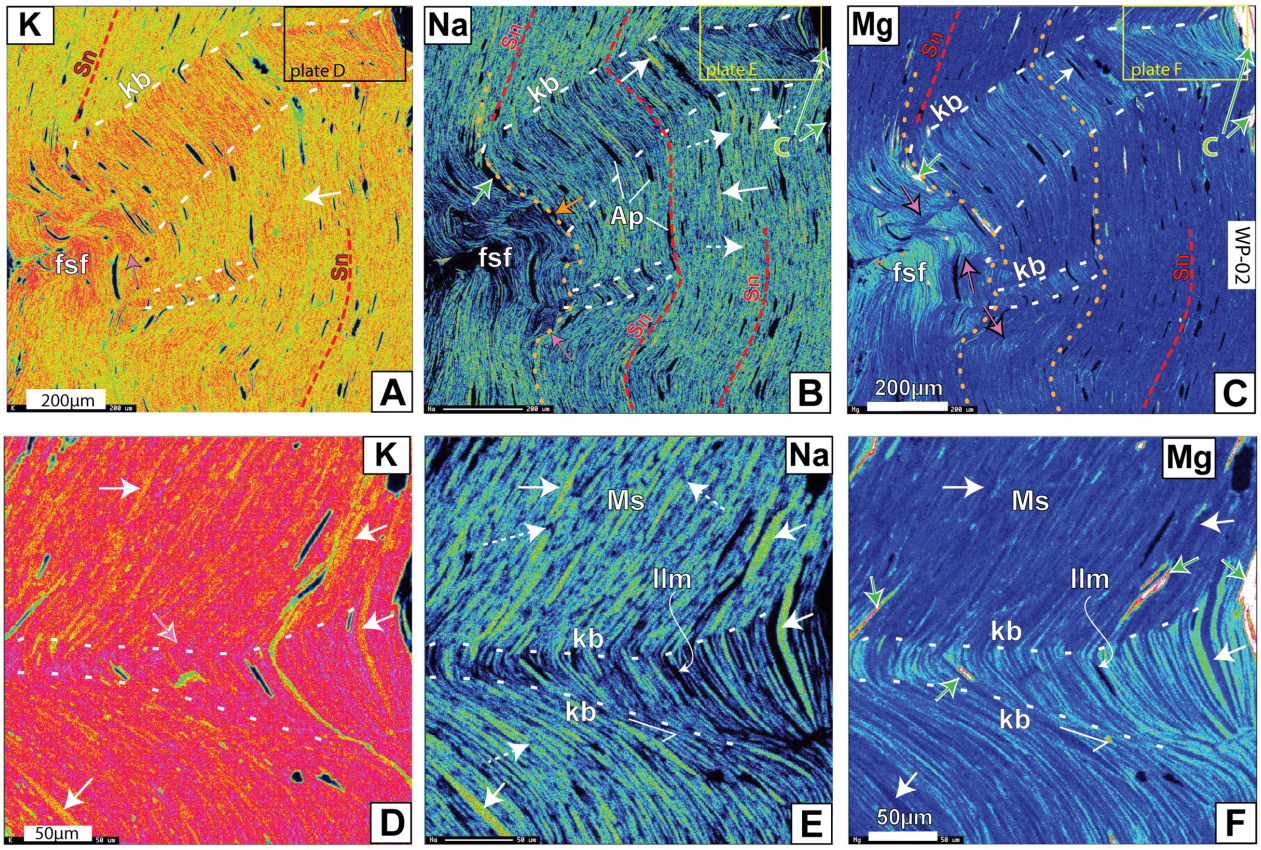

Figure 11. K, Na, and Mg element maps showing details of muscovite from kinked folds in sample WP-02 (fig. 8). Kink-band boundaries are identified with dashed white lines. Green arrows identify chlorite (C), and white arrows identify relic Na-rich muscovite flakes. (A), (B), and (C) show that muscovite flakes in the short, overturned limbs of the kink folds are richer in K (red, plate A), poorer in Na (dark blue, plate B), and richer in Mg (pale blue, plate C). The region of complicated folding (fsf) is especially thoroughly recrystallized. Boxes show the location of panels D, E, and F. (D), (E), (F) Details of the images in A, B, and C, showing (1) relic Na-rich muscovite flakes (white arrows) sandwiched between Na-poor and Mg richer muscovite blades, and (2) selective recrystallization of muscovite in the kink band to Na-poor and Mg-rich compositions.

necks contain < 7% pg (fig. 6C). In sample WP-29 a longer muscovite grain shows at least four steps of falling pg content from a maximum of ~35% in the core to < 5% in the boudin neck and beards (fig. 6E; table S7). Reference to the pg contours of figure 3 shows that this boudinage occurred during falling metamorphic temperatures with pg concentrations > 15% (yellow field) recording Acadian deformation, whereas boudin necks and beards crystallized during Alleghanian deformation (orange field, fig. 6E). Another example is shown in figure 4H, where steps are marked by dashed lines in the graphed compositions. These boundaries are not conspicuous in the BSE of figure 6G (analyses 1–7) suggesting crystallographic continuity across the steps in this grain.

4.5.3. *GRAIN BOUNDARY SLIDING*

Grain boundary sliding (GBS) textures are very common in these phyllonites (figs. 4–12). GBS surfaces separate any combination of muscovite-rich folia, quartz ribbons, microlithons, relic porphyroblasts, and their pseudomorphs. Perhaps the most dramatic example is in sample WP-02 (fig. 8). Here the folds on the left side of figure 8A are out of phase and terminate abruptly against straight muscovite folia, quartz ribbons, and against each other.

4.5.4. *FLEXURAL SLIP FOLDS AND KINK BANDS*

Folds and kink bands occur in many samples at scales > 100µm (figs. 4A, B, 6A, 7–9, 12) to scales of <50 µm (figs. 6B–D, 11). Most folds are kink folds, but isoclinal folds also occur (figs. 7, 9, S3). Kink folds may occur in sets (e.g., fig. S3) and generally die out within a few half wavelengths of the short limb. For example, in figure 6A between X and X' kinks are bounded by sliding surfaces between muscovite and quartz ribbons (fig. 6A). Similar surfaces enclose kinks in figures 6B–D, 8A, 11, and S3.

These observations show that flexural slip was important in the development of kink folds, such as in figure 7, although they likely began as incipient kink bands with parallel dislocation loops (Basu et al., 2009). Here the limbs of the fold slid down (barbed arrows) toward the fold hinge, truncating folia in their footwalls, including straight muscovite flakes in the nose at 'X'. The Mg element map (fig.

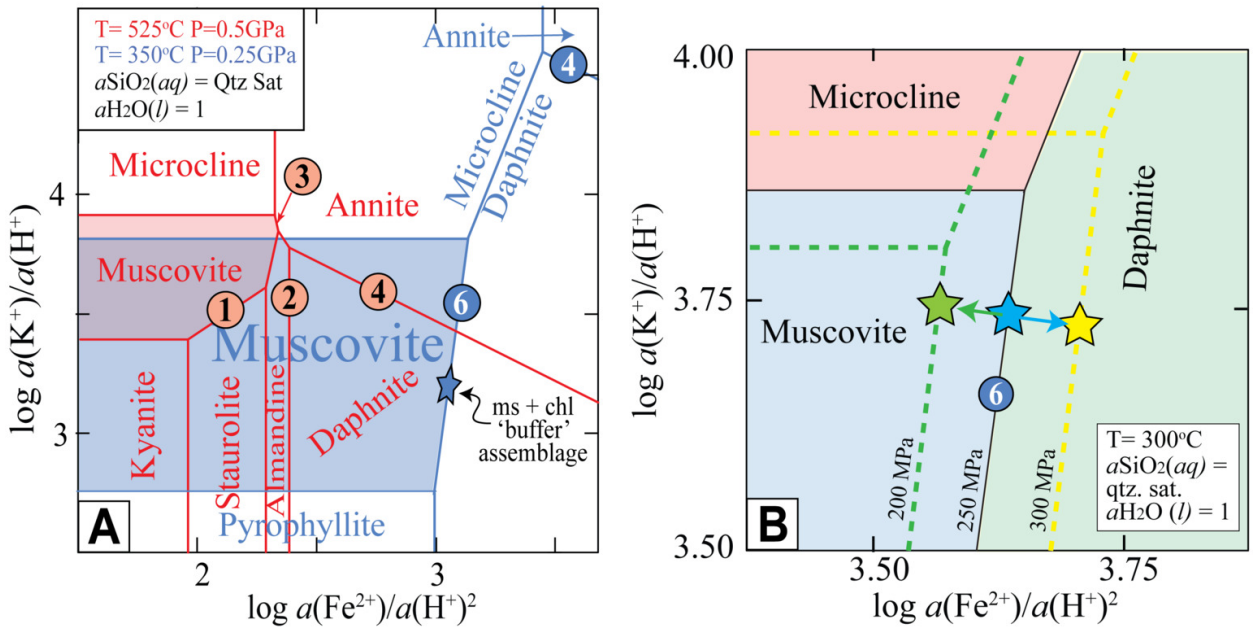

Figure 12. (A) An aqueous activity diagram calculated using SUPCRTBL (Zimmer et al., 2016) showing two superimposed diagrams reflecting the metamorphic conditions near the PTt path of the Wepawaug Schist and the EDsz (red stars fig. 3). The circled numbers refer to the reactions in Table 1. At high-grade conditions muscovite is stable with all minerals except chlorite. At low-grade the muscovite field expands greatly, and the only mafic mineral in equilibrium with muscovite is daphnite. (B) Aqueous activity diagram showing the effect of pressure on the size of the stability field of muscovite (blue) relative to that of daphnite (green) and microcline (pink) at 300 °C.

7B) shows that the limbs are nearly chlorite-free, whereas the hinge of the fold contains chevron-shaped domains of chlorite (red and white). The noses of kink folds shown in figure 6B are similarly filled with chlorite, as are the cores of synforms in figure 8. We interpret this microstructure to reflect dissolution and removal of chlorite (± muscovite) from the limbs of the fold and precipitation of chlorite in the extensional sites in the fold noses in "saddle reef" -like structures. Where flexural slip did not lead to extension in the fold hinge, but to contraction, crenulation is unusually intense. The crenulated folds in sample WP-02 led to selective recrystallization of pg-rich muscovite to pg-poor compositions (especially clear in fig. 11C). The core in the synform in figure 6D (red/white arrow) is similarly recrystallized.

4.5.5. DISLOCATION GLIDE

Microstructures unambiguously supporting the operation of basal dislocation glide in phyllosilicates are rare. One example could be deformed Na-rich muscovite flakes in fig. 4E. There, the wide white arrow (upper right) points to a splintered Na-rich muscovite flake that could be explained by dislocation glide in the basal plane. Other candidates for dislocation glide (e.g., wide white arrow, fig. 6C) might also be explained by GBS. However, evidence for abundant dislocation glide is not strong.

4.6. $^{40}Ar/^{39}Ar$ geochronology

$^{40}Ar/^{39}Ar$ geochronology is used to compare the apparent ages of muscovite in high-grade assemblages with those in the phyllonites. Two domains in staurolite-grade sample WP-162 (fig. 6A) from the western margin of the shear zone (fig. 2) were analyzed. One domain contained continuous Sn foliation (inside pink dotted line, fig 6A), and the second contained crenulated Sn (inside green dotted line). Detailed imaging and corresponding EMPA of muscovite show that the undeformed muscovite is relatively sodic (>15 % pg, figs. 6B, C). However, deformed grains, especially in overturned limbs of kink bands contain muscovite with <10 % pg. The age spectrum produced by muscovite from the continuous Sn foliation yielded a plateau age of ~ 367 ± 4 Ma (fig. 9). Muscovite from the crenulated domain (green circled area, fig. 6A) produced a similar plateau age of 366 ± 4 Ma (2σ).

To compare this result with the apparent ages of recrystallized muscovite with pg concentrations < 11% from within the EDsz, we analyzed muscovite from two foliations from sample WP-045E (fig. 9). An earlier foliation containing coarse muscovite (flakes > 100μm long) with chlorite and minor albite occurs in microlithons as folded Sn-1 (dashed yellow lines, figs 9A–C). A second foliation containing finer grained muscovite (< 50μm long) defines Sn (red dashed lines in fig. 9) with Na contents <~10% pg (fig. 10). Coarse muscovite flakes interpreted to represent Sn-1 and fine-grained composite flakes of muscovite from the truncating Sn cleavage were handpicked for analysis. An

aliquot of several coarse flakes produced a sigmoidal age spectrum with age steps ranging from ~296 to ~314 Ma, with a total gas age of ~304 Ma. The finer grained muscovite flakes produced an age spectrum with steps climbing from ~265 to ~280 Ma with a total gas age of ~270 Ma (fig. 9).

5. DISCUSSION

The above observations help to identify the primary processes producing cleavages in the EDsz. The metamorphic context for the history of these rocks is important and is constrained in part on the Ar isotopic data. We begin the discussion below with the isotopic results that help establish the P-T-time path by establishing the time of cooling of the protolith rocks and the duration of the zone's residence under greenschist facies conditions.

5.1. $^{40}Ar/^{39}Ar$ isotopic analysis

The cooling history of the Wepawaug Schist establishes the context for the thermal history of the relic minerals in the EDsz. Amphibole cooling ages of ~375 Ma are available from Growdon et al. (2013), and a muscovite cooling age of ~365 Ma is established above and discussed in Supplementary Information. Calculated closure temperatures for these minerals are 544 ºC and 391 ºC, respectively (Reiners & Brandon, 2006; see Supplementary Information). These data constrain the PTt path for these rocks (horizontal boxes, fig. 3B). The age spectra from phyllonitic sample WP-45E thus record approximate ages of crystallization of retrograde muscovite.

5.2. PTt path

The retrograde portion of the calculated PTt path of figure 3B is constrained to pass through the Late Devonian hornblende and muscovite closure temperatures, and to remain in greenschist facies conditions through the Permian as required by the crystallization ages of phyllonitic muscovite. This path constrains the PT conditions of Acadian foliations and of fabric development in phyllonites (blue field, fig. 3B) It is remarkably similar to the path presented by Wolfe et al. (2021) for correlative rocks in Vermont.

5.3. Reaction mechanisms

The reactions described in section 4.4 all involve aqueous species. The mechanism of these reactions was thus one of dissolution, diffusive transfer, and precipitation. This process is equally germane to petrology as a metamorphic reaction mechanism (Carmichael, 1969) and to structural geology: pressure solution (Gratier et al., 2013), although the former is driven by reaction overstepping (Pattison et al., 2011), whereas the latter is driven by the energy dissipated from inelastic deformation (Hobbs et al., 2010). The implied presence of H_2O in the grain boundary is significant because it acts as a catalyst lowering the activation energy barriers for dissolution, diffusive transfer, nucleation, precipitation, and growth (Putnis, 2021). These steps were involved in both the static replacement reactions and the cleavage-forming reactions.

5.3.1. STATIC REPLACEMENT REACTIONS

The retrograde reactions involving the replacement of staurolite and garnet (reactions 1 and 2, table 1) require the introduction of H_2O and produce volume increases. These alteration reactions could thus be driven by an increase in the activity of H_2O and by a drop in pressure. The replacement of biotite by chlorite (reaction 3, table 1) similarly requires the introduction of H^+ but involves a volume reduction. The association of muscovite + chlorite with all three reactions indicates that the replacements occurred under lower greenschist facies conditions. At these low-grade conditions these Acadian reactant minerals are metastable with their stability fields replaced by muscovite and chlorite (fig. 12A). This metastability provided the activation energy to drive the replacement reactions, a form of reaction overstepping (e.g., Pattison et al., 2011; Wolfe & Spear, 2018).

The survival of muscovite with high pg contents in the phyllonites is unique among relic Acadian minerals. The green contours of figure 3A show that muscovite with >~15% pg content is metastable with respect to a less sodic muscovite at temperatures < 350 ºC. For such an overstep in composition (ΔX) the activation energy, or reaction affinity (A) of Pattison et al. (2011) is expressed by the relationship: $A = RT(\Delta \ln a)$ where $\Delta \ln a = \ln a - \ln a_{eq}$ (where the subscript eq refers to the equilibrium activity). Apparently, the magnitude of overstepping based on composition (e.g., reaction 7, table 1) is insufficient to drive its replacement, as is typical of low Δ entropy reactions (Pattison et al., 2011).

5.3.2. CLEAVAGE-FORMING REACTIONS

Muscovite is the primary fabric-forming mineral in the phyllonites of the EDsz. In every microstructure a younger muscovite-bearing cleavage truncates an earlier foliation. This process involves either the dissolution of the minerals in the truncated structure, or the precipitation of muscovite in the truncating structure, or both. In each case muscovite in the younger cleavage defines a new and strong foliation. This strong foliation indicates that the process was syn-tectonic.

Reactions 5 and 6 involving the replacement of biotite and chlorite by muscovite can be driven by an increase in acidity, and given the large negative volume changes, also by a high normal stress. However, the microstructures show that the replacement of muscovite by muscovite (no. 7, table 1) is probably the most penetrative reaction producing new cleavages. Typically, pg-rich muscovite flakes are truncated by pg-poor muscovite blades (figs. 4E, 6C, 7C, 8E), but pg-poor muscovite is also truncated in more thoroughly recrystallized folia (figs. 4E, 6C, and especially figs. 9, 10).

Less common is the truncation of pg-poor muscovite and chlorite by pg-rich muscovite (figs. 4G, S4). The ΔV is positive, so a high normal stress cannot explain the driving force for this reaction, and the chemical affinity is opposite that of reaction overstepping. Our interpretation is that the

Na-rich muscovite grain was in a strong orientation with the (00l) planes at a high angle to the shortening direction and remained undeformed, whereas the (00l) planes of muscovite flakes in truncated microstructures were in orientations sub parallel to the shortening direction where elastic and plastic strain energy in the bent grains drove their dissolution (Hobbs et al., 2010). Thus, pressure solution must have been involved (section 5.5.1).

5.4. Deformation mechanisms: pressure solution

Of the several deformation mechanisms identified in this study (section 4.5), pressure solution is the most important. GBS is also important and is a necessary consequence of diffusion creep at the grain scale (McClay, 1977; Stevens, 1971). However, we find abundant evidence for GBS on discrete surfaces at a multi-grain scale (section 4.5.2.). Microstructural evidence for the dominance of pressure solution comes from (1) the truncation of grains in earlier cleavages, including muscovite, chlorite, biotite, and locally quartz and plagioclase (figs. 4–10), and (2) the precipitation of new muscovite grains that define new cleavages (many images) with new tetrahedral and octahedral compositions (e.g., figs. 6, 10; Supplementary information). More evidence for muscovite precipitation comes from the multiple muscovite overgrowths on a pg-rich muscovite boudin (fig. 6E). New, crosscutting folia tend to have very little chlorite, even though the components of chlorite are clearly available to precipitate. Figures 4, 7–10 show muscovite folia devoid of chlorite but also show the precipitation of chlorite in extensional sites, especially fold hinges (figs. 5B, 7B, and 8). The precipitation of chlorite in these folds allowed the fold amplitudes to grow (fig. 8). These relationships show that the sites of dissolution may be decoupled from the sites of precipitation, requiring diffusive transfer.

The driving force for pressure solution is the strain energy in the deformed grains (e.g. Gratier et al., 2013; Hobbs et al., 2010). Support for this interpretation comes from the selective recrystallization of bent or kinked muscovite grains in microfolds described in section 4.4.2. EMPA data demonstrating changes in composition confirm this recrystallization. The pg contents of muscovite across the set of crenulations in the upper left of figure S3 oscillate between >20% and <15% in the long and short limbs of kinks. The short limb of the small kink band of figure 6C recrystallized to muscovite with 7% pg from precursor muscovite with 18% pg. Muscovite in the overturned limbs on the kink folds of figure 8 (stars) are also pg-poor (~10% pg) but host a relic muscovite blade of 27% pg (fig. 8C, D, E). These examples demonstrate that the elastic strain in muscovite, probably also associated with dislocations (I. A. Bell et al., 1986) and perhaps other high energy defects (Barber et al., 2010; Brantley et al., 1986; Engelder, 1982; M. R. Lee & Parsons, 1995; Wenk et al., 2008) provided enough energy to drive recrystallization.

The replacement of chlorite by muscovite (reaction 6, table 1) can be best assessed through use of aqueous activity diagrams that show the effect of pressure on the boundaries of their stability fields. An increase in pressure from 250 MPa to 300 MPa moves the muscovite-chlorite field boundary to the right to solutions with a higher $a(Fe^{2+})/a(H^+)^2$ ratio (dashed yellow line, fig. 12B). To maintain equilibrium a solution would have to increase its $\alpha(Fe^{2+})/\alpha(H^+)^2$ ratio from the composition of the blue star to that of the yellow star in figure 12B. To accomplish this chlorite must dissolve, and following reaction 6 (table 1) the solution composition will move to the lower right following the blue arrow with a slope of - 2/15. This relationship describes most of the textures defining new muscovite cleavages described here.

The opposite situation occurs with a decrease in pressure. In this situation the solution composition must lower its $\alpha\ (Fe^{2+})/\ \alpha\ (H^+)^2$ ratio from compositions of the blue star to that of the green star (fig. 13B). In this case chlorite must precipitate, removing Fe^{2+} from solution and the solution composition will move along a path of the green arrow. If differential stress exists in a microstructure, then sites of local high and low pressure will exist at the same time. Thus, in sites of high normal stress chlorite will dissolve and muscovite may precipitate, while in sites of low normal stress chlorite will precipitate. This describes both the redistribution of chlorite from the limbs to the hinges of folds in figures 7 and 8, and the pressure solution process in general.

6. A PRESSURE SOLUTION MODEL FOR THE EVOLUTION OF CLEAVAGES IN THE EDSZ

The above observations are assembled as a conceptual model in figure 13. E-W Alleghanian shortening provides the context for the steep foliations in the diagram. The earliest fabric depicted (identified as Sn-2) is an Acadian composite foliation (T. H. Bell & Newman, 2006) of muscovite (ocher) and biotite (brown) that occurs in microlithons (ML, figs. 4, 9) and as quartz and ilmenite inclusion trails in some pseudomorphed porphyroblasts (left side, fig. 4). Muscovite in an early Alleghanian composite foliation, Sn-1 (yellow dashed lines) with moderate pg content (apple green) contains relic wafers (W) and lenses of pg -rich muscovite and rarely biotite (brown) as documented in figures 4–8. Sn-1 also contains lenses of albite (the by-product of reaction 7, table 1) and blades of ilmenite.

A younger Alleghanian foliation (Sn, red dashed lines, most figs.) is defined by pg -poor muscovite (sky blue). Clusters of Sn muscovite blades may contain some relic wedges of pg-richer muscovite and biotite (yellow and brown, respectively). Sn also defines the axial planes of folded Sn-1 (center). Sn is locally crenulated with sub-horizontal axial planes defining Sn+1 (bright blue dashed lines, right side of fig. 13). A pseudomorph of randomly oriented muscovite after staurolite [St] is sandwiched within Sn folia. A few randomly oriented muscovite blades (long white rectangles) cut all other structures (e.g., black double arrows in fig. 9C). These are probably associated with the late static pseudomorphic event. These many generations of muscovite create an array of muscovite age populations

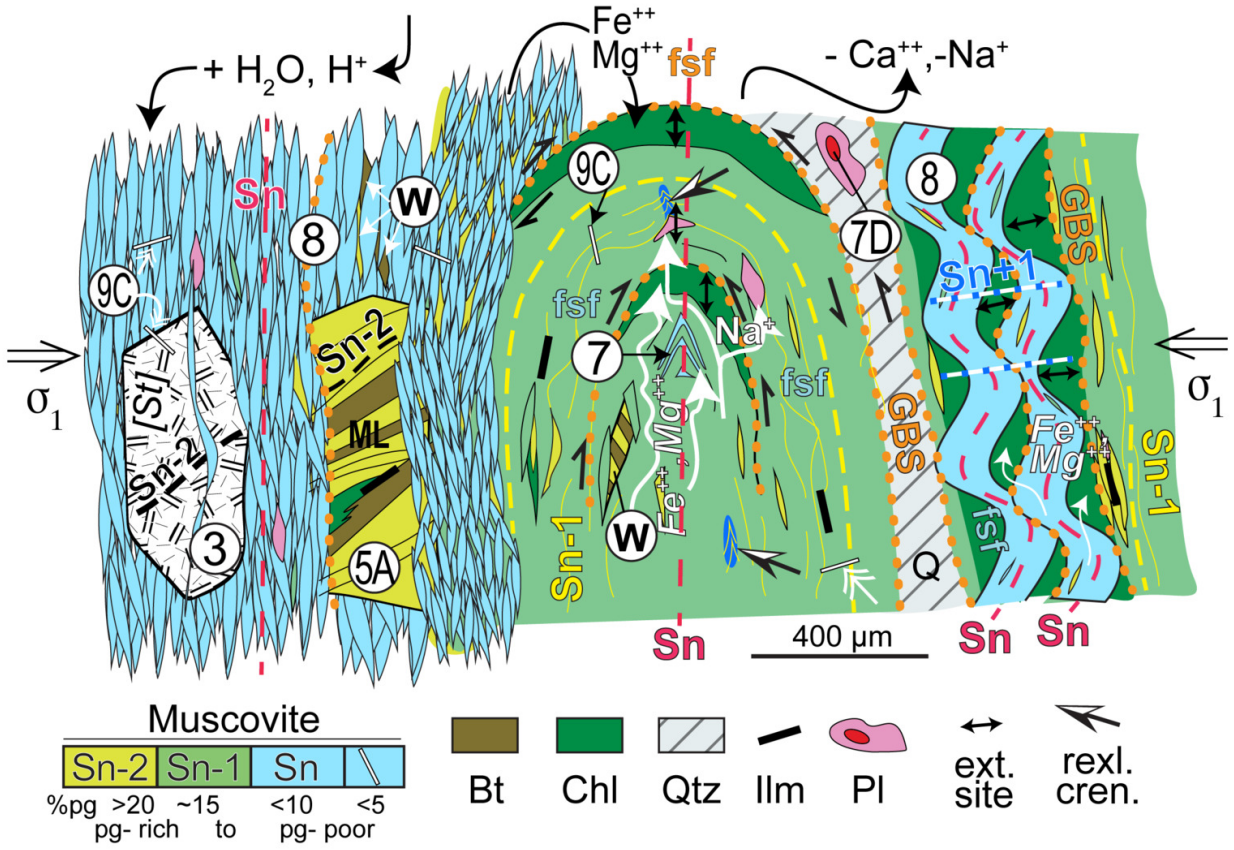

Figure 13. A schematic diagram summarizing the fabric-forming processes identified in the EDsz. Circled numbers refer to figures after which the microstructures were modeled. Relic Acadian foliation (Sn-2) contains Na-rich muscovite and biotite (5A). An early Alleghanian fabric (Sn-1, dashed yellow line) is composed of muscovite with moderate Na content (pale green) with minor chlorite (dark green), ilmenite (black blades, Ilm), and albite (pink). The latter replaces older plagioclase with a higher An content (7D). It may also include relic wedges (W) of Acadian muscovite and biotite. A younger Alleghanian cleavage, Sn, (red dashed lines) defined almost exclusively by Na-poor muscovite (sky blue) cuts all other structures. It contains a few relic grains of chlorite, albite, and older Na-rich (yellow) muscovite. Sn deformation is axial planar to folded Sn-1 (figure center). Sn truncates most other structures and can penetrate muscovite pseudomorphs after staurolite (3). Sn+1 locally crenulates other fabrics, producing fold trains (8). Areas around tight crenulations (bright blue) are selectively recrystallized (black/white arrows, figs. 6D, 11). The latest randomly oriented flakes of muscovite (white laths, 9C) cut all structures. Pressure solution dissolves earlier muscovite, biotite, and chlorite in earlier cleavages, and leads to increasingly pure muscovite folia with decreasing Na contents (yellow to green to blue). The reactions progress in a system partially open to the addition of H_2O, to the loss of Ca^{++} and Na^{+}, and to the diffusive transfer of Fe^{++}, Mg^{++}, and Na^{+} (white arrows) to extensional sites where chlorite and albite precipitate. For other discussion, refer to text.

that probably accounts for the disturbed age spectra of the two younger $^{40}Ar/^{39}Ar$ age spectra of fig. 9D.

Differential stress between σ_1 and σ_3 created a standing chemical potential gradient in the electric double layer that coats the grain boundary network in mineral aggregates (e.g., Hickman & Evans, 1991; Moore & Lockner, 2004; Schott et al., 2009; Spiers et al., 2004). This gradient drove the diffusive transfer of dissolved cations of chlorite and pg-rich muscovite (white arrows, fig. 13) from the limbs to the hinges of this fold (black double-headed arrows) where they precipitated as chlorite (figs. 6A, B, 7B, 8) and albite (fig. 9C). The precipitation of chlorite in fold noses facilitated flexural slip folding (fsf) that increased fold amplitudes. The same precipitation of chlorite allowed the train of disharmonic folds (right side, fig. 13) to grow in amplitude and GBS between the trains put them out of phase.

7. TECTONIC SIGNIFICANCE

7.1. Fabric development

Muscovite flakes with (00l) planes in orientations sub-parallel to S1 tend to dissolve against flakes in strong orientations with (00l) planes normal to S1. Folding of earlier folia would bring those phyllosilicates into relatively weak orientations where the strain energy added by folding and associated dislocations (Bons, 1988) would make them more soluble and susceptible to dissolution and selective replace-

ment (figs. 4, 5, 8–10). This conclusion is consistent with deformation-induced recrystallization in general (Chapman et al., 2019; Giuntoli et al., 2018; Hobbs et al., 2010; Koons et al., 1987; McWilliams et al., 2007; Moecher & Wintsch, 1994; Putnis, 2021; Wintsch & Andrews, 1988). It is also possible that the far-field shortening direction rotated because the approaching Gondwana plate rotated clockwise during the Alleghanian orogeny (Hatcher, 2002; Pastor-Galán, 2022; Wintsch & Lefort, 1984; fig. 1A). It is likely that diffusion creep was activated at lower stresses than dislocation creep, making the latter less important (Stöckhert et al., 1999).

The selective dissolution of chlorite from some folia and precipitation in adjacent folia has led to mineralogical banding. In this case the less soluble muscovite precipitated locally in the actively growing cleavage folia, whereas the components of the more soluble chlorite migrated to extensional sites where they precipitated as new chlorite. This concentrated muscovite grains at sites of high normal stress in some samples (figs. 4G, 7) and produced mineralogical banding in others (e.g., figs. 9, 10). Such differential solubilities of minerals in deforming mineral aggregates might be an explanation for metamorphic differentiation in many settings (Putnis, 2002).

7.2. Displacement and stretching fault

Displacement across the EDsz is difficult to prove because it lies largely within the Wepawaug Schist (fig. 2). The evidence for any displacement on the EDsz comes from the truncation of the contact between the Wepawaug Schist and the Maltby Lakes Metavolcanics near sample WP-124, and the truncation of isograds in the wall rocks on its NW and SE margins (fig. 2). On the other hand, the southern increase in metamorphic grade on both sides of the EDsz requires a differential vertical stretch increasing to the south. Indeed, kilometer-scale telescoping of the isograds has been identified (Growdon et al., 2013), and the lack of horizontal displacement requires the telescoping to be largely vertical. This telescoping fits the properties of stretching faults or stretching shear zones (Bailey et al., 2004; Fossen & Cavalcante, 2017; Means, 1989) and is the best explanation available for the occurrence of phyllonites in the EDsz.

The location and trend of the ED-DP shear zone was probably controlled by structural inheritance along the eastern margin of Laurentia in the early Paleozoic. This margin was established during late Neoproterozoic (Aleinikoff et al., 1995; Cawood & Nemchin, 2001; Li et al., 2008) rifting of the supercontinent Rodinia that produced a series of rifts offset by intervening transform faults (fig. 1A; Thomas, 2006). One such rift produced the New York promontory that established a headland along the Laurentian margin. This relatively thick, cool, and thus strong crust acted as a buttress that localized deformation during several succeeding orogenic accretionary events (Long, 2024). The latest Alleghanian event affected much of SE New England where Pennsylvanian and Permian metamorphism overprinted Acadian metamorphic rocks in most of eastern Connecticut (e.g., Wintsch et al., 2014; Zartman et al., 1970). The EDsz marks the western margin of rocks thoroughly recrystallized during the Alleghanian orogeny, where its deformation accommodated NW-SE shortening and helped to localize late Paleozoic strain that generally did not penetrate farther west into the Acadian buttress.

8. CONCLUSIONS

In this study of the EDsz, we find evidence that pressure solution and GBS were the dominant deformation mechanisms operating in these phyllonites. This evidence includes (1) dissolution of relic Acadian high-grade pg-rich muscovite from the Wepawaug Schist protolith, (2) precipitation of new pg-poor muscovite ± chlorite selectively in the younger cleavages, (3) precipitation of only muscovite in the latest cleavages, (4) the precipitation of chlorite in extensional sites, and (5) up to mm scale GBS facilitated by the dissolution of grains in truncated folia. Where cleavage-forming muscovite replaced muscovite flakes with (001) orientations at a high angle to the shortening direction, the strain energy in the deformed grains drove their selective dissolution, whereas the selective dissolution of chlorite was probably also driven by its higher solubility relative to muscovite. This study supports the observation of Putnis (2021) that the sites of dissolution and precipitation may be decoupled. This decoupling is at the core of the metamorphic differentiation in the phyllonites found in these rocks, and selective or differential solubility contributed to this metamorphic differentiation.

The deformation mechanism operating in these phyllonites is one of dissolution-diffusive mass transfer, and precipitation or pressure solution and concomitant grain boundary sliding leading to flow by diffusion creep. This is contrary to the predictions of experimental studies that dislocation glide should be the dominant deformation mechanism in muscovite. The implication is that diffusion creep with GBS is activated at lower differential stresses than those causing dislocation creep. If this is true, the operation of these deformation mechanisms would limit the differential stresses to values below that necessary to activate dislocation creep. These processes may also be responsible for mitigating against the higher stresses necessary to produce earthquakes.

ACKNOWLEDGMENTS

We have benefitted over the years from discussions about chemo-mechanical feedback and cleavages with many colleagues including Brian Bayly, Rob Knipe, Tony Lanzirotti, Win Means, and Don Wise. We also gratefully acknowledge more recent discussions with Jay Ague, Chuck Bailey, Tim Bell, Dave Bish, Bruce Hobbs, Andeas Kronenberg, Harvey Belkin, Mick Kunk, Andre Niemeijer, Alison Ord, Andrew Putnis, Chris Spiers, John Waldron, Greg Walsh, and Chen Zhu. Ryan Deasy and Chris Helou assisted in the field and in the lab, Chusi Li helped with preliminary electron microprobe analyses at Indiana University, and IU Librarian Jian Liu helped find hard to acquire articles in libraries oth-

erwise closed by COVID. BW thanks the Calhoun family for lodging in the field. Financial assistance to BW from the Department of Earth and Atmospheric Sciences at Indiana University and the Geological Society of Connecticut is gratefully acknowledged. We thank Laura Airaghi, Harvey Belkin, Dave Bish, Ryan Deasy, Lisa Eberhard, Andreas Kronenberg, Sandra Piazolo, Andrew Putnis, Phil Resor, Guillaume Siron, Rebecca Stokes, and Chen Zhu for helpful suggestions that improved earlier drafts. Further comments and editorial handling by Mark Brandon are greatly appreciated. Any use of trade, firm, or product names is for descriptive purposes only and does not imply endorsement by the U.S. Government.

AUTHOR CONTRIBUTIONS

All authors contributed to ideas, metamorphic context, and to the writing of selected passages in this manuscript. B.W. completed the field work, and performed the initial petrography, microprobe analysis, Ar sample preparation, and wrote an early draft. R.M. completed the Ar isotopic analysis and executed detailed microprobe analysis. J.W. calculated and interpreted the pseudosection calculations. J.M. provided metamorphic context for the regional geology. R.W. prepared the final manuscript with contributions from B.W., R.M., and J.W.

Supplementary Information

https://doi.org/10.5281/zenodo.13896245

Editor: Mark Brandon, Associate Editor: Lucie Tajcmanova

Submitted: January 21, 2022 EST, Accepted: July 29, 2024 EST

REFERENCES

Ague, J. J. (1994a). Mass transfer during Barrovian metamorphism of pelites, south-central Connecticut; I, Evidence for changes in composition and volume. *American Journal of Science*, *294*(8), 989–1057. https://doi.org/10.2475/ajs.294.8.989

Ague, J. J. (1994b). Mass transfer during Barrovian metamorphism of pelites, south-central Connecticut; II, Channelized fluid flow and the growth of staurolite and kyanite. *American Journal of Science*, *294*(9), 1061–1134. https://doi.org/10.2475/ajs.294.9.1061

Ague, J. J. (2002). Gradients in fluid composition across metacarbonate layers of the Wepawaug Schist, Connecticut, USA. *Contributions to Mineralogy and Petrology*, *143*(1), 38–55. https://doi.org/10.1007/s00410-001-0330-9

Airaghi, L., Lanari, P., de Sigoyer, J., & Guillot, S. (2017). Microstructural vs compositional preservation and pseudomorphic replacement of muscovite in deformed metapelites from the Longmen Shan (Sichuan, China). *Lithos*, *282–283*, 262–280. https://doi.org/10.1016/j.lithos.2017.03.013

Aleinikoff, J. N., Zartman, R. E., Walter, M., Rankin, D. W., Lyttle, P. T., & Burton, W. C. (1995). U-Pb ages of metarhyolites of the Catoctin and Mount Rogers formations, Central and Southern Appalachians; evidence for two pulses of Iapetan rifting. *American Journal of Science*, *295*(4), 428–454. https://doi.org/10.2475/ajs.295.4.428

Bailey, C. M., Francis, B. E., & Fahrney, E. E. (2004). Strain and vorticity analysis of transpressional high-strain zones from the Virginia Piedmont, USA. *Geological Society, London, Special Publications*, *224*(1), 249–264. https://doi.org/10.1144/GSL.SP.2004.224.01.16

Barber, D. J., Wenk, H.-R., Hirth, G., & Kohlstedt, D. L. (2010). Chapter 95 Dislocations in Minerals. In *Dislocations in Solids* (pp. 171–232). https://doi.org/10.1016/s1572-4859(09)01604-0

Basu, S., Zhou, A., & Barsoum, M. W. (2009). On spherical nanoindentations, kinking nonlinear elasticity of mica single crystals and their geological implications. *Journal of Structural Geology*, *31*(8), 791–801. https://doi.org/10.1016/j.jsg.2009.05.008

Beaudoin, A., Scaillet, S., Mora, N., Jolivet, L., & Augier, R. (2020). In situ and step-Heating 40Ar/39Ar dating of white mica in low-temperature shear zones (Tenda Massif, Alpine Corsica, France). *Tectonics*, *39*(12), e2020TC006246. https://doi.org/10.1029/2020TC006246

Bell, I. A., Wilson, C. J. L., McLaren, A. C., & Etheridge, M. A. (1986). Kinks in mica: role of dislocations and (001) cleavage. *Tectonophysics*, *127*(1–2), 49–65. https://doi.org/10.1016/0040-1951(86)90078-8

Bell, T. H., & Newman, R. (2006). Appalachian orogenesis: the role of repeated gravitational collapse. *Styles of Continental Contraction*. https://doi.org/10.1130/2006.2414(06)

Bons, A.-J. (1988). Deformation of chlorite in naturally deformed low-grade rocks. *Tectonophysics*, *154*(1–2), 149–165. https://doi.org/10.1016/0040-1951(88)90232-6

Brantley, S. L., Crane, S. R., Crerar, D. A., Hellmann, R., & Stallard, R. (1986). Dissolution at dislocation etch pits in quartz. *Geochimica et Cosmochimica Acta*, *50*(10), 2349–2361. https://doi.org/10.1016/0016-7037(86)90087-6

Carmichael, D. M. (1969). On the mechanism of prograde metamorphic reactions in quartz-bearing pelitic rocks. *Contributions to Mineralogy and Petrology*, *20*(3), 244–267. https://doi.org/10.1007/BF00377479

Cawood, P. A., & Nemchin, A. A. (2001). Paleogeographic development of the east Laurentian margin: Constraints from U-Pb dating of detrital zircons in the Newfoundland Appalachians. *Geological Society of America Bulletin*, *113*(9), 1234–1246. https://doi.org/10.1130/0016-7606%282001%29113%3C1234%3APDOTEL%3E2.0.CO%3B2

Ceccato, A., Goncalves, P., & Menegon, L. (2022). On the petrology and microstructures of small-scale ductile shear zones in granitoid rocks: an overview. *Journal of Structural Geology*, *161*, 104667. https://doi.org/10.1016/j.jsg.2022.104667

Chapman, T., Clarke, G. L., Piazolo, S., Robbins, V. A., & Trimby, P. W. (2019). Grain-scale dependency of metamorphic reaction on crystal plastic strain. *Journal of Metamorphic Geology*, *37*, 1021–1036. https://doi.org/10.1111/jmg.12473

Clark, G. S., & Kulp, J. L. (1968). Isotopic age study of metamorphism and intrusion in western Connecticut and southeastern New York. *American Journal of Science*, *266*(10), 865–894. https://doi.org/10.2475/ajs.266.10.865

Connolly, J. A. D. (2005). Computation of phase equilibria by linear programming: a tool for geodynamic modeling and its application to subduction zone decarbonation. *Earth and Planetary Science Letters*, *236*(1–2), 524–541. https://doi.org/10.1016/j.epsl.2005.04.033

Connolly, J. A. D. (2009). The geodynamic equation of state: what and how. *Geochemistry, Geophysics, Geosystems*, *10*(10). https://doi.org/10.1029/2009gc002540

Dabrowski, D., & Evans, M. (2009). Fluid inclusion microthermometry of quartz veins from the Wepawaug Schist, southern Connecticut. *Geological Society of America Abstracts with Programs*, *41*(3), 110.

De Caroli, S., Fagereng, Å., Ujiie, K., Blenkinsop, T., Meneghini, F., & Muir, D. (2024). Deformation microstructures of low- and high-strain epidote-blueschist (Ryukyu arc, Japan): Implications for subduction interface rheology. *Journal of Structural Geology*, *180*, 105041. https://doi.org/10.1016/j.jsg.2023.105041

Deasy, R. T., Wathen, B. A., & Wintsch, R. P. (2017). Bedrock geology of the Paleozoic rocks of western New Haven quadrangle, Connecticut. *Journal of Maps*, *13*(2), 632–643. https://doi.org/10.1080/17445647.2017.1348308

Diener, J. F., Fagereng, Å., & Thomas, S. A. J. (2016). Mid-crustal shear zone development under retrograde conditions: pressure–temperature–fluid constraints from the Kuckaus Mylonite Zone, Namibia. *Solid Earth*, *7*(5), 1331–1347. https://doi.org/10.5194/se-7-1331-2016

Dietsch, C., Kunk, M. J., Aleinikoff, J., & Sutter, J. F. (2010). *The tectono-thermal evolution of the Waterbury dome, western Connecticut, based on U-Pb and 40Ar/39Ar ages: From Rodinia to Pangea: The Lithotectonic Record of the Appalachian Region*. https://doi.org/10.1130/2010.1206(08)

Engelder, T. (1982). A natural example of the simultaneous operation of free-face dissolution and pressure solution. *Geochimica et Cosmochimica Acta*, *46*(1), 69–74. https://doi.org/10.1016/0016-7037(82)90291-5

England, P. C., & Thompson, A. B. (1984). Pressure—temperature—time paths of regional metamorphism I. Heat transfer during the evolution of regions of thickened continental crust. *Journal of Petrology*, *25*(4), 894–928. https://doi.org/10.1093/petrology/25.4.894

Fossen, H., & Cavalcante, G. C. G. (2017). Shear zones – A review. *Earth-Science Reviews*, *171*, 434–455. https://doi.org/10.1016/j.earscirev.2017.05.002

Fritts, C. E. (1962). Age and sequence of metasedimentary and metavolcanic formations northwest of New Haven, Connecticut. *U.S. Geological Survey Professional Paper*, *450*, D32–D36.

Fritts, C. E. (1965). *Bedrock geologic map of the Ansonia quadrangle, Fairfield and New Haven Counties, Connecticut*. U.S. Geological Survey, Geological Quadrangle Map GQ 426. https://doi.org/10.3133/gq426

Giuntoli, F., Menegon, L., & Warren, C. J. (2018). Replacement reactions and deformation by dissolution and precipitation processes in amphibolites. *Journal of Metamorphic Geology*, *36*(9), 1263–1286. https://doi.org/10.1111/jmg.12445

Gratier, J.-P., Dysthe, D. K., & Renard, F. (2013). The role of pressure solution creep in the ductility of the Earth's upper crust. *Advances in Geophysics*, *54*, 47–179. https://doi.org/10.1016/B978-0-12-380940-7.00002-0

Growdon, M. L., Kunk, M. J., Wintsch, R. P., & Walsh, G. J. (2013). Telescoping metamorphic isograds: Evidence from 40Ar/39Ar dating in the Orange-Milford belt, southern Connecticut. *American Journal of Science*, *313*(10), 1017–1053. https://doi.org/10.2475/10.2013.03

Hatch, N. L., & Stanley, R. S. (1973). *Some suggested stratigraphic relations in part of southwestern New England*. U.S. Geological Survey, Bulletin 1380.

Hatcher, R. D., Jr. (2002). Alleghanian (Appalachian) orogeny, a product of zipper tectonics: Rotational transpressive continent-continent collision and closing of ancient oceans along irregular margins. In *Variscan-Appalachian dynamics: The building of the late Paleozoic basement*. https://doi.org/10.1130/0-8137-2364-7.199

Haugerud, R. A. (1989). On numerical modeling of one-dimensional geothermal histories. *Computers & Geosciences*, *15*(5), 825–836. https://doi.org/10.1016/0098-3004(89)90084-8

Hibbard, J. P., van Staal, C. R., Rankin, D. W., & Williams, H. (2006). *Lithotectonic map of the Appalachian orogen (South), Canada-United States of America* (2 Sheets, Scale 1:1,500,000 No. 02096A). Geological Survey of Canada Map.

Hickman, S. H., & Evans, B. (1991). Experimental pressure solution in halite: the effect of grain/interphase boundary structure. *Journal of the Geological Society*, *148*(3), 549–560. https://doi.org/10.1144/gsjgs.148.3.0549

Hillenbrand, I., Williams, M. L., Jercinovic, M. J., Heizler, M. T., & Tjapkes, D. J. (2023). Petrochronologic constraints on Paleozoic tectonics in southern New England. *Laurentia: Turning Points in the Evolution of a Continent*. https://doi.org/10.1130/2022.1220(25)

Hillenbrand, I., Williams, M., Peterman, E., Jercinovic, M. J., & Dietsch, C. (2024). Petrochronologic Constraints on Inverted Metamorphism, Terrane Accretion, Thrust Stacking, and Ductile Flow in the Gneiss Dome Belt, Northern Appalachian Orogen. *Geological Society of America Abstracts with Programs*, *56*(1). https://doi.org/10.1130/abs/2024ne-397436

Hobbs, B. E., Ord, A., Spalla, M. I., Gosso, G., & Zucali, M. (2010). The interaction of deformation and metamorphic reactions. *Geological Society, London, Special Publications*, *332*(1), 189–223. https://doi.org/10.1144/SP332.12

Holland, T. J. B., & Powell, R. (2011). An improved and extended internally consistent thermodynamic dataset for phases of petrological interest, involving a new equation of state for solids. *Journal of Metamorphic Geology*, *29*(3), 333–383. https://doi.org/10.1111/j.1525-1314.2010.00923.x

Koons, P. O., Rubie, D. C., & Fruch-Green, G. (1987). The effects of disequilibrium and deformation on the mineralogical evolution of quartz diorite during metamorphism in the eclogite facies. *Journal of Petrology*, *28*(4), 679–700. https://doi.org/10.1093/petrology/28.4.679

Kronenberg, A. K., Kirby, S. H., & Pinkston, J. (1990). Basal slip and mechanical anisotropy of biotite. *Journal of Geophysical Research: Solid Earth*, *95*(B12), 19257–19278. https://doi.org/10.1029/JB095iB12p19257

Lancaster, P. J., Baxter, E. F., Ague, J. J., Breeding, C. M., & Owens, T. L. (2008). Synchronous peak Barrovian metamorphism driven by syn-orogenic magmatism and fluid flow in southern Connecticut, USA. *Journal of Metamorphic Geology*, *26*(5), 527–538. https://doi.org/10.1111/j.1525-1314.2008.00773.x

Lanzirotti, A., & Hanson, G. N. (1995). U-Pb dating of major and accessory minerals formed during metamorphism and deformation of metapelites. *Geochimica et Cosmochimica Acta*, *59*(12), 2513–2526. https://doi.org/10.1016/0016-7037(95)00146-8

Lanzirotti, A., & Hanson, G. N. (1996). Geochronology and geochemistry of multiple generations of monazite from the Wepawaug Schist, Connecticut, USA: implications for monazite stability in metamorphic rocks. *Contributions to Mineralogy and Petrology*, *125*(4), 322–340. https://doi.org/10.1007/s004100050226

Lanzirotti, A., & Hanson, G. N. (1997). An assessment of the utility of staurolite in U-Pb dating of metamorphism. *Contributions to Mineralogy and Petrology*, *129*(4), 352–365. https://doi.org/10.1007/s004100050342

Lee, A. L., Stünitz, H., Soret, M., & Battisti, M. A. (2022). Dissolution precipitation creep as a process for the strain localization in mafic rocks. *Journal of Structural Geology*, *155*, 104505. https://doi.org/10.1016/j.jsg.2021.104505

Lee, M. R., & Parsons, I. (1995). Microtextural controls of weathering of perthitic alkali feldspars. *Geochimica et Cosmochimica Acta*, *59*(21), 4465–4488. https://doi.org/10.1016/0016-7037(95)00255-X

Li, Z. X., Bogdanova, S. V., Collins, A. S., Davidson, A., De Waele, B., Ernst, R. E., Fitzsimons, I. C. W., Fuck, R. A., Gladkochub, D. P., Jacobs, J., Karlstrom, K. E., Lu, S., Natapov, L. M., Pease, V., Pisarevsky, S. A., Thrane, K., & Vernikovsky, V. (2008). Assembly, configuration, and break-up history of Rodinia: a synthesis. *Precambrian Research*, *160*(1–2), 179–210. https://doi.org/10.1016/j.precamres.2007.04.021

Long, M. D. (2024). Evolution, Modification, and Deformation of Continental Lithosphere: Insights from the Eastern Margin of North America. *Annual Review of Earth and Planetary Sciences*, *52*(1), 549–580. https://doi.org/10.1146/annurev-earth-040522-115229

Ludwig, K. R. (2012). *User's Manual for Isoplot 3.75, A Geochronological Toolkit for Microsoft Excel* (p. 75). Berkeley Geochronology Center, Special Publication 5.

Mares, V. M., & Kronenberg, A. K. (1993). Experimental deformation of muscovite. *Journal of Structural Geology*, *15*(9–10), 1061–1075. https://doi.org/10.1016/0191-8141(93)90156-5

Mariani, E., Brodie, K. H., & Rutter, E. H. (2006). Experimental deformation of muscovite shear zones at high temperatures under hydrothermal conditions and the strength of phyllosilicate-bearing faults in nature. *Journal of Structural Geology*, *28*(9), 1569–1587. https://doi.org/10.1016/j.jsg.2006.06.009

Matthews, J. A., Wintsch, R. P., & Simmons, W. M. (2008). Regional metamorphic history and exhumation of the southern Connecticut Valley Synclinorium, southwestern Connecticut. *Geological Society of America, Abstracts with Programs*, *40*(2), 61.

McAleer, R. J., Bish, D. L., Kunk, M. J., Sicard, K. R., Valley, P. M., Walsh, G. J., Wathen, B. A., & Wintsch, R. P. (2017). Reaction softening by dissolution–precipitation creep in a retrograde greenschist facies ductile shear zone, New Hampshire, USA. *Journal of Metamorphic Geology*, *35*(1), 95–119. https://doi.org/10.1111/jmg.12222

McClay, K. R. (1977). Pressure solution and Coble creep in rocks and minerals: a review. *Journal of the Geological Society*, *134*(1), 57–70. https://doi.org/10.1144/gsjgs.134.1.0057

McNamara, D. D., Wheeler, J., Pearce, M., & Prior, D. J. (2024). A key role for diffusion creep in eclogites: Omphacite deformation in the Zermatt-Saas unit, Italian Alps. *Journal of Structural Geology*, *179*, 105033. https://doi.org/10.1016/j.jsg.2023.105033

McWilliams, C. K., Kunk, M. J., Wintsch, R. P., & Bish, D. L. (2013). Determining ages of multiple muscovite-bearing foliations in phyllonites using the 40Ar/39Ar step heating method: Applications to the Alleghanian Orogeny in Central New England. *American Journal of Science*, *313*(10), 996–1016. https://doi.org/10.2475/10.2013.02

McWilliams, C. K., Wintsch, R. P., & Kunk, M. J. (2007). Scales of equilibrium and disequilibrium during cleavage formation in chlorite and biotite-grade phyllites, SE Vermont. *Journal of Metamorphic Geology*, *25*(8), 895–913. https://doi.org/10.1111/j.1525-1314.2007.00734.x

Means, W. D. (1989). Stretching faults. *Geology*, *17*(10), 893–896. https://doi.org/10.1130/0091-7613%281989%29017%3C0893%3ASF%3E2.3.CO%3B2

Moecher, D. P., Cosca, M. A., & Hanson, G. N. (1997). Petrologic and 40Ar/39Ar geochronological constraints on the middle to late Paleozoic thermotectonic history of the southern Connecticut Valley zone, New England Appalachians. *Geological Society of America Bulletin*, *109*(2), 164–175. https://doi.org/10.1130/0016-7606%281997%29109%3C0164%3APAAAGC%3E2.3.CO%3B2

Moecher, D. P., & Wintsch, R. P. (1994). Deformation-induced reconstitution and local resetting of mineral equilibria in polymetamorphic gneisses: tectonic and metamorphic implications. *Journal of Metamorphic Geology*, *12*(4), 523–538. https://doi.org/10.1111/j.1525-1314.1994.tb00040.x

Moore, D. E., & Lockner, D. A. (2004). Crystallographic controls on the frictional behavior of dry and water-saturated sheet structure minerals. *Journal of Geophysical Research: Solid Earth*, *109(B3)*. https://doi.org/10.1029/2003JB002582

Newman, R. L. (2001). *Inter-relationships between metamorphism and deformation during Acadian orogenesis in SW Connecticut* [PhD thesis]. James Cook University.

Nosenzo, F., Manzotti, P., & Robyr, M. (2023). H2O budget and metamorphic re-equilibration in polycyclic rocks as recorded by garnet textures and chemistry. *Lithos*, *452–453*, 107230. https://doi.org/10.1016/j.lithos.2023.107230

Oriolo, S., Schulz, B., Hueck, M., Oyhantçabal, P., Heidelbach, F., Sosa, G., van den Kerkhof, A., Wemmer, K., Fossen, H., Druguet, E., Walter, J., Cavalcante, C., & Siegesmund, S. (2022). The petrologic and petrochronologic record of progressive vs polyphase deformation: Opening the analytical toolbox. *Earth-Science Reviews*, *234*, 104235. https://doi.org/10.1016/j.earscirev.2022.104235

Passchier, C. W., & Trouw, R. (2005). *Microtectonics*. Springer Science & Business Media.

Pastor-Galán, D. (2022). From supercontinent to superplate: Late Paleozoic Pangea's inner deformation suggests it was a short-lived superplate. *Earth-Science Reviews*, *226*, 103918. https://doi.org/10.1016/j.earscirev.2022.103918

Pattison, D. R. M., De Capitani, C., & Gaidies, F. (2011). Petrological consequences of variations in metamorphic reaction affinity. *Journal of Metamorphic Geology*, *29*(9), 953–977. https://doi.org/10.1111/j.1525-1314.2011.00950.x

Putnis, A. (2002). Mineral replacement reactions: from macroscopic observations to microscopic mechanisms. *Mineralogical Magazine*, *66*(5), 689–708. https://doi.org/10.1180/0026461026650056

Putnis, A. (2021). Fluid–Mineral Interactions: Controlling Coupled Mechanisms of Reaction, Mass Transfer and Deformation. *Journal of Petrology*, *62*(12), egab092. https://doi.org/10.1093/petrology/egab092

Reiners, P. W., & Brandon, M. T. (2006). Using thermochronology to understand orogenic erosion. *Annual Review of Earth and Planetary Sciences*, *34*(1), 419–466. https://doi.org/10.1146/annurev.earth.34.031405.125202

Rodgers, J. (1985). *Bedrock Geological Map of Connecticut* [Scale 1: 125,000]. Connecticut Geological and Natural History Survey, Department of Environmental Protection, Hartford, Connecticut. http://www.ct.gov/deep

Rutter, E. H. (1983). Pressure solution in nature, theory and experiment. *Journal of the Geological Society*, *140*(5), 725–740. https://doi.org/10.1144/gsjgs.140.5.0725

Samsu, A., Micklethwaite, S., Williams, J. N., Fagereng, Å., & Cruden, A. R. (2023). Structural inheritance in amagmatic rift basins: Manifestations and mechanisms for how pre-existing structures influence rift-related faults. *Earth-Science Reviews*, *246*, 104568. https://doi.org/10.1016/j.earscirev.2023.104568

Scharf, A., Handy, M. R., Favaro, S., Schmid, S. M., & Bertrand, A. (2013). Modes of orogen-parallel stretching and extensional exhumation in response to microplate indentation and roll-back subduction (Tauern Window, Eastern Alps). *International Journal of Earth Sciences*, *102*(6), 1627–1654. https://doi.org/10.1007/s00531-013-0894-4

Schott, J., Pokrovsky, O. S., & Oelkers, E. H. (2009). The Link Between Mineral Dissolution/ Precipitation Kinetics and Solution Chemistry: In Thermodynamics and Kinetics of Water-Rock Interaction. *Mineralogical Society of America, Reviews in Mineralogy and Geochemistry*, *70*(1), 207–258. https://doi.org/10.2138/rmg.2009.70.6

Sevigny, J. H., & Hanson, G. N. (1993). Orogenic evolution of the New England Appalachians of southwestern Connecticut. *Geological Society of America Bulletin*, *105*(12), 1591–1605. https://doi.org/10.1130/0016-7606%281993%29105%3C1591%3AOEOTNE%3E2.3.CO%3B2

Sevigny, J. H., & Hanson, G. N. (1995). Late-Taconian and pre-Acadian history of the New England Appalachians of southwestern Connecticut. *Geological Society of America Bulletin*, *107*(4), 487–498. https://doi.org/10.1130/0016-7606%281995%29107%3C0487%3ALTAPAH%3E2.3.CO%3B2

Shea, W. T., & Kronenberg, A. K. (1992). Rheology and deformation mechanisms of an isotropic mica schist. *Journal of Geophysical Research: Solid Earth*, *97*(B11), 15201–15237. https://doi.org/10.1029/92JB00620

Shea, W. T., & Kronenberg, A. K. (1993). Strength and anisotropy of foliated rocks with varied mica contents. *Journal of Structural Geology*, *15*(9–10), 1097–1121. https://doi.org/10.1016/0191-8141(93)90158-7

Spear, F. S. (1995). Metamorphic phase equilibria and pressure-temperature-time paths. *Mineralogical Society of America Monograph*, 352.

Spiers, C. J., De Meer, S., Niemeijer, A. R., & Zhang, X. (2004). Kinetics of rock deformation by pressure solution and the role of thin aqueous films. In S. Nakashima, C. J. Spiers, L. Mercury, P. A. Fenter, & M. F. Hocheller Jr. (Eds.), *Physicochemistry of Water in Geological and Biological Systems: Structures and Properties of Thin Aqueous Films* (pp. 129–158). Universal Academy Press.

Stenvall, C. A., Fagereng, A., Diener, J. F. A., Harris, C., & Janney, P. E. (2020). Sources and Effects of Fluids in Continental Retrograde Shear Zones: Insights from the Kuckaus Mylonite Zone, Namibia. *Geofluids*, 3023268. https://doi.org/10.1155/2020/3023268

Stevens, R. N. (1971). Grain-boundary sliding and diffusion creep in polycrystalline solids. *Philosophical Magazine*, *23*(182), 265–283. https://doi.org/10.1080/14786437108216383

Stöckhert, B., Wachmann, M., Küster, M., & Bimmermann, S. (1999). Low effective viscosity during high pressure metamorphism due to dissolution precipitation creep: the record of HP–LT metamorphic carbonates and siliciclastic rocks from Crete. *Tectonophysics*, *303*(1–4), 299–319. https://doi.org/10.1016/S0040-1951(98)00262-5

Tenczer, V., Powell, R., & Stüwe, K. (2006). Evolution of H2O content in a polymetamorphic terrane: the Plattengneiss Shear Zone (Koralpe, Austria). *Journal of Metamorphic Geology*, *24*(4), 281–295. https://doi.org/10.1111/j.1525-1314.2006.00637.x

Thomas, W. A. (2006). Tectonic inheritance at a continental margin. *GSA Today*, *16*(2), 4–11. https://doi.org/10.1130/1052-5173%282006%29016[4%3Atiaacm]2.0.co%3B2

Tokle, L., Hirth, G., & Stünitz, H. (2023). The effect of muscovite on the microstructural evolution and rheology of quartzite in general shear. *Journal of Structural Geology*, *169*, 104835. https://doi.org/10.1016/j.jsg.2023.104835

Torgersen, E., Gabrielsen, R. H., Ganerød, M., van der Lelij, R., Schönenberger, J., Nystuen, J. P., & Brask, S. (2022). Repeated brittle reactivations of a pre-existing plastic shear zone: combined K–Ar and 40Ar–39Ar geochronology of the long-lived (> 700 Ma) Himdalen–Ørje Deformation Zone, SE Norway. *Geological Magazine*, *159*(11–12), 2110–2131. https://doi.org/10.1017/s0016756822000966

Tulley, C. J., Fagereng, Å., Ujiie, K., Diener, J. F. A., & Harris, C. (2022). Embrittlement within viscous shear zones across the base of the subduction thrust seismogenic zone. *Geochemistry, Geophysics, Geosystems*, *23*(9), e2021GC010208. https://doi.org/10.1029/2021GC010208

Villa, I. M., Glodny, J., Peillod, A., Skelton, A., & Ring, U. (2023). Petrochronology of polygenetic white micas (Naxos, Greece). *Journal of Metamorphic Geology*, *41*(3), 401–423. https://doi.org/10.1111/jmg.12700

Wallis, D., Lloyd, G. E., Phillips, R. J., Parsons, A. J., & Walshaw, R. D. (2015). Low effective fault strength due to frictional-viscous flow in phyllonites, Karakoram Fault Zone, NW India. *Journal of Structural Geology*, *77*, 45–61. https://doi.org/10.1016/j.jsg.2015.05.010

Wathen, B. A. (2020). *Deformation and recrystallization in the development of a retrograde shear zone* (M.S. Thesis No. 28257959). Indiana University.

Wathen, B. A., Helou, C., Wintsch, R. P., Deasy, R. T., Yi, K., McAleer, R., & Matthews, J. (2015). Deformation spanning 200 million years along the peri-Laurentian (Pumpkin Ground Orthogneiss) Buttress and the East Derby Shear Zone, South-central Connecticut. In M. S. Gilmore & P. G. Resor (Eds.), *Guidebook to field trips in Connecticut and Massachusetts* (pp. 153–172). Wesleyan University.

Wenk, H.-R., Monteiro, P. J., & Shomglin, K. (2008). Relationship between aggregate microstructure and mortar expansion. A case study of deformed granitic rocks from the Santa Rosa mylonite zone. *Journal of Materials Science*, *43*, 1278–1285. https://doi.org/10.1007/s10853-007-2175-8

Wenk, H.-R., Yu, R., Cárdenes, V., Lopez-Sanchez, M. A., & Sintubin, M. (2020). Fabric and anisotropy of slates: From classical studies to new results. *Journal of Structural Geology*, *138*, 104066. https://doi.org/10.1016/j.jsg.2020.104066

Wheeler, G. (1937). The West Wall of the New England Triassic Lowland. *State Geological and Natural History Survey of Connecticut, Bulletin*, *58*.

White, S. H., & Johnston, D. C. (1981). A microstructural and microchemical study of cleavage lamellae in a slate. *Journal of Structural Geology*, *3*(3), 279–290. https://doi.org/10.1016/0191-8141(81)90023-7

Wiest, J. D., Fossen, H., & Jacobs, J. (2020). Shear zone evolution during core complex exhumation – Implications for continental detachments. *Journal of Structural Geology*, *140*, 104139. https://doi.org/10.1016/j.jsg.2020.104139

Wintsch, R. P., Aleinikoff, J. N., & Yi, K. (2005). Foliation development and reaction softening by dissolution and precipitation in the transformation of granodiorite to orthogneiss, Glastonbury Complex, Connecticut, U.S.A. *The Canadian Mineralogist*, *43*(1), 327–347. https://doi.org/10.2113/gscanmin.43.1.327

Wintsch, R. P., & Andrews, M. S. (1988). Deformation induced growth of sillimanite: "Stress" minerals revisited. *The Journal of Geology*, *96*(2), 143–161. https://doi.org/10.1086/629206

Wintsch, R. P., Christoffersen, R., & Kronenberg, A. K. (1995). Fluid-rock reaction weakening of fault zones. *Journal of Geophysical Research: Solid Earth*, *100*(B7), 13021–13032. https://doi.org/10.1029/94JB02622

Wintsch, R. P., & Lefort, J. P. (1984). A clockwise rotation of Variscan strain orientation in SE New England and regional implications. *Geological Society, London, Special Publications*, *14*(1), 245–251. https://doi.org/10.1144/GSL.SP.1984.014.01.22

Wintsch, R. P., Roden-Tice, M., Kunk, M. J., & Aleinikoff, J. N. (2003). Ductile to brittle Mesozoic overprint of Alleghanian structures, Bronson Hill terrane, Rockville area, Connecticut. In *Field Trip Guidebook of the 84th Annual New England Intercollegiate Geologic Conference* (pp. A3-31).

Wintsch, R. P., Sutter, J. F., Kunk, M. J., Aleinikoff, J. N., & Dorais, M. J. (1992). Contrasting P-T-t paths: Thermochronologic evidence for a Late Paleozoic final assembly of the Avalon Composite Terrane in the New England Appalachians. *Tectonics*, *11*(3), 672–689. https://doi.org/10.1029/91TC02904

Wintsch, R. P., Wathen, B. A., McAleer, R. J., Walters, J., & Matthews, J. A. (2024). Electron Microprobe and 40Ar/39Ar data from the East Derby Shear Zone, Connecticut. *U.S. Geological Survey Data Release*. https://doi.org/10.5066/P9ZL6GK6

Wintsch, R. P., & Yi, K. (2002). Dissolution and replacement creep: a significant deformation mechanism in mid-crustal rocks. *Journal of Structural Geology*, *24*(6–7), 1179–1193. https://doi.org/10.1016/S0191-8141(01)00100-6

Wintsch, R. P., Yi, K., & Dorais, M. J. (2014). Crustal thickening by tectonic wedging of the Ganderian rocks, southern New England, USA: evidence from cataclastic zircon microstructures and U–Pb ages. *Journal of Structural Geology*, *69*, 428–448. https://doi.org/10.1016/j.jsg.2014.07.019

Wintsch, R. P., Yi, K., Kim, S. J., Lee, S., & Devlin, W. (2017). A Silurian depositional age and mixed eastern and western provenance for the Straits Schist confirmed by detrital zircon geochronology. *Geological Society of America Abstracts with Programs*, *49*(2). https://doi.org/10.1130/abs/2017NE-290643

Wolfe, O. M., & Spear, F. S. (2018). Determining the amount of overstepping required to nucleate garnet during Barrovian regional metamorphism, Connecticut Valley Synclinorium. *Journal of Metamorphic Geology*, *36*(1), 79–94. https://doi.org/10.1111/jmg.12284

Wolfe, O. M., Spear, F. S., & Harrison, T. M. (2021). Pronounced and rapid exhumation of the Connecticut Valley Trough revealed through quartz in garnet Raman barometry and diffusion modelling of garnet dissolution–reprecipitation reactions. *Journal of Metamorphic Geology*, *39*(8), 1045–1069. https://doi.org/10.1111/jmg.12601

Zartman, R. E., Hurley, P. M., Krueger, H. W., & Giletti, B. J. (1970). A Permian disturbance of K-Ar radiometric ages in New England: its occurrence and cause. *Geological Society of America Bulletin*, *81*(11), 3359–3374. https://doi.org/10.1130/0016-7606%281970%2981[3359%3AAPDOKR]2.0.CO%3B2

Zimmer, K., Zhang, Y., Lu, P., Chen, Y., Zhang, G., Dalkilic, M., & Zhu, C. (2016). SUPCRTBL: A revised and extended thermodynamic dataset and software package of SUPCRT92. *Computers & Geosciences*, *90*, 97–111. https://doi.org/10.1016/j.cageo.2016.02.013

SUPPLEMENTARY MATERIALS

Supplementary Information

Download: https://ajsonline.org/article/125064-deformation-by-pressure-solution-and-grain-boundary-sliding-in-a-retrograde-shear-zone-in-southern-new-england-usa/attachment/251612.docx

Supplementary Information Table S5

Download: https://ajsonline.org/article/125064-deformation-by-pressure-solution-and-grain-boundary-sliding-in-a-retrograde-shear-zone-in-southern-new-england-usa/attachment/251613.xlsx

Supplementary Information Table S8

Download: https://ajsonline.org/article/125064-deformation-by-pressure-solution-and-grain-boundary-sliding-in-a-retrograde-shear-zone-in-southern-new-england-usa/attachment/251614.xlsx